

# Symmetry-breaking Hopf bifurcations to 1-, 2-, and 3-tori in small-aspect-ratio counterrotating Taylor-Couette flow

S. Altmeyer and Y. Do

*Department of Mathematics, Kyungpook National University, Daegu 702-701, Korea*

F. Marques

*Department of Física Aplicada, Universitat Politècnica de Catalunya, Girona s/n, Mòdul B4 Campus Nord, 08034 Barcelona, Spain*

J. M. Lopez\*

*School of Mathematical and Statistical Sciences, Arizona State University, Tempe, Arizona 85287, USA and*

*Department of Mathematics, Kyungpook National University, Daegu 702-701, Korea*

(Received 10 August 2012; published 18 October 2012)

The nonlinear dynamics of Taylor-Couette flow in a small-aspect-ratio wide-gap annulus in the counterrotating regime is investigated by solving the full three-dimensional Navier-Stokes equations. The system is invariant under arbitrary rotations about the axis, reflection about the annulus midplane, and time translations. A systematic investigation is presented both in terms of the flow physics elucidated from the numerical simulations and from a dynamical system perspective provided by equivariant normal form theory. The dynamics are primarily associated with the behavior of the jet of angular momentum that emerges from the inner cylinder boundary layer at about the midplane. The sequence of bifurcations as the differential rotation is increased consists of an axisymmetric Hopf bifurcation breaking the reflection symmetry of the basic state leading to an axisymmetric limit cycle with a half-period-flip spatiotemporal symmetry. This undergoes a Hopf bifurcation breaking axisymmetry, leading to quasiperiodic solutions evolving on a 2-torus that is setwise symmetric. These undergo a further Hopf bifurcation, introducing a third incommensurate frequency leading to a 3-torus that is also setwise symmetric. On the 3-torus, as the differential rotation is further increased, a saddle-node-invariant-circle bifurcation takes place, destroying the 3-torus and leaving a pair of symmetrically related 2-tori states on which all symmetries of the system have been broken.

DOI: [10.1103/PhysRevE.86.046316](https://doi.org/10.1103/PhysRevE.86.046316)

PACS number(s): 47.20.Ky, 47.32.cf, 47.54.—

## I. INTRODUCTION

The transition from two-dimensional to three-dimensional flows in hydrodynamics is a fundamental step towards turbulence. There are numerous situations where the two-dimensional state is time periodic and has symmetries additional to the invariance in the third direction. One example is the flow between two concentric differentially rotating cylinders, Taylor-Couette flow, which has played a central role in the development of hydrodynamic stability theory [1,2]. Its geometric simplicity allows for well-controlled experiments. Theoretical progress originally proceeded by making the geometric idealizations of an infinite aspect ratio of the annulus ( $\Gamma$ , the ratio of cylinder lengths to the annular gap), where the axial direction is treated as being periodic, and the ratio of the radii of the two cylinders approaching 1, diminishing the effects of curvature.

Numerous numerical and experimental investigations have shown that the effects of physical end walls are not negligible [3–5] even in very long Taylor-Couette systems (large  $\Gamma$ ) and have a significant influence on the flow dynamics. The presence of end walls, even in the limit of being infinitely far apart, completely destroys the axial translation invariance in the idealized theory. A direct consequence of destroying the continuous translation symmetry due to the presence of end

walls is that instead of a continuous spectrum of axial wave numbers only a discrete one approximately exists for very large aspect ratios and for very small aspect ratios the concept of axial periodicity is lost.

In the classical setup with the inner cylinder rotating and the outer cylinder stationary, the flow dynamics for small systems  $\Gamma \approx 1$  is dominated by the competition between several normal and anomalous modes leading to very rich dynamics [4,6–11]. For very short systems only one or two Taylor cells are present [12,13].

In the counterrotating cylinders case, there are very few results in the short-aspect-ratio regime. The early experiments considered large aspect ratios [14] and often radius ratios close to 1 [15], primarily in order to accommodate the approximations and idealizations that were being made in the contemporary theoretical studies [16]. More recently, there has been much interest in this regime as it supports localized turbulent patches, referred to as spiral turbulence, which appear to be a result of shear instability due to the strong counterrotation [15,17–25]. In contrast, there are virtually no results in the regime of a very short aspect ratio with a wide gap. The results of the present study will show that the flow dynamics in this regime are dominated by the centrifugal instability of the inner cylinder boundary layer and the associated jet of angular momentum issuing out of it.

One of the very few studies of short-aspect-ratio wide-gap counterrotating Taylor-Couette flow is Schulz *et al.* [13], who considered aspect ratios in the range  $\Gamma \in [0.96, 1.28]$ . They

\*jmlopez@asu.edu

conducted both experiments and numerical simulations in regimes where steady flows with either one or two axisymmetric cells occur. Their numerical techniques were restricted to solving the steady axisymmetric Navier-Stokes equations and they focused on the axisymmetric pitchfork bifurcation between the (reflection-symmetric) two-cell branch of solutions and the (reflection-symmetry-broken) one-cell branch. Within this framework, they determined that counterrotation of the two cylinders promotes breaking the reflection symmetry. However, their restricted analysis leaves open the question of other symmetry-breaking and time-dependent instabilities of the basic state in this often overlooked regime.

In this paper we investigate numerically the dynamics of Taylor-Couette flow using a time-dependent three-dimensional Navier-Stokes spectral solver and consider a one-parameter path of increasing inner cylinder rotation rate while the counterrotating outer cylinder's rotation rate is held fixed. The chosen parameter path cuts through the heart of the region where the flow dynamics is dominated by centrifugal instability and is primarily associated with the behavior of the jet of angular momentum that emerges from the inner cylinder boundary layer at about the midplane combined with interactions with secondary jets. Various symmetry-breaking Hopf bifurcations result in a sequence of periodic and quasiperiodic solutions. At small  $Re_i$ , the steady symmetric basic state loses stability in a supercritical Hopf bifurcation that breaks the reflection symmetry and leads to an axisymmetric limit cycle with half-period-flip symmetry. On further increasing  $Re_i$ , this limit cycle loses stability in an axisymmetry-breaking Hopf bifurcation, introducing a second (incommensurate) frequency associated with a mean precession in the azimuthal direction, resulting in a quasiperiodic solution on a 2-torus invariant manifold. For higher  $Re_i$ , a further Hopf bifurcation introduces a third frequency and spawns quasiperiodic solutions on a 3-torus manifold. Both the 2-torus and 3-torus, as sets, possess the full symmetry of the system; however, the respective quasiperiodic solutions do not. Increasing  $Re_i$  on the 3-torus branch leads to the third frequency vanishing in a saddle-node-invariant-circle (SNIC) bifurcation and following this bifurcation 2-torus states result. These 2-torus states are no longer setwise reflection symmetric; the SNIC bifurcation here is a setwise symmetry-breaking bifurcation. The quasiperiodic solutions on these 2-tori have all symmetries of the system broken. Flow features of these various solutions branches are described in terms of both their flow physics and equivariant normal form theory.

## II. GOVERNING EQUATIONS

Consider the flow driven in the annular gap between two independently rotating cylinders of length  $L$ . The inner cylinder of radius  $R_i$  rotates at angular speed  $\Omega_i$  and the outer cylinder of radius  $R_o$  rotates at angular speed  $\Omega_o$ . The end walls enclosing the annulus are stationary. The fluid in the annulus is considered to be Newtonian, isothermal, and incompressible with kinematic viscosity  $\nu$ . Using the gap  $R_o - R_i$  as the length scale and the radial diffusion time  $(R_o - R_i)^2/\nu$  as the time scale, the nondimensional Navier-Stokes equations governing the flow are

$$\partial_t \mathbf{u} + (\mathbf{u} \cdot \nabla) \mathbf{u} = -\nabla p + \nabla^2 \mathbf{u}, \quad \nabla \cdot \mathbf{u} = 0, \quad (1)$$

where  $\mathbf{u} = (u, v, w)$  is the velocity in cylindrical coordinates  $(r, \theta, z)$  and the corresponding vorticity is  $\nabla \times \mathbf{u} = (\xi, \eta, \zeta)$ . The system is governed by four parameters: the inner and outer Reynolds numbers  $Re_i = \Omega_i R_i (R_o - R_i)/\nu$  and  $Re_o = \Omega_o R_o (R_o - R_i)/\nu$ , the aspect ratio  $\Gamma = L/(R_o - R_i)$ , and the radius ratio  $R_i/R_o$ . The boundary conditions are no slip, with  $\mathbf{u}(r_i, \theta, z, t) = (0, Re_i, 0)$ ,  $\mathbf{u}(r_o, \theta, z, t) = (0, Re_o, 0)$ , and  $\mathbf{u}(r, \theta, \pm 0.5\Gamma, t) = (0, 0, 0)$ , where the nondimensional inner and outer radii are  $r_i = R_i/(R_o - R_i)$  and  $r_o = R_o/(R_o - R_i)$ .

The governing equations and the boundary conditions are invariant under arbitrary rotations  $R_\alpha$  about the axis, reflection  $K_z$  about the annulus midplane  $z = 0$ , and time translations  $\phi_{t_0}$ , generating the symmetry group  $SO(2) \times Z_2 \times \mathbb{R}$ , where the first two factors consist of the purely spatial symmetries, while the third factor corresponds to the temporal symmetries generating the one-dimensional translation group  $\mathbb{R}$ . The actions of the three symmetries on the velocity are

$$R_\alpha(u, v, w)(r, \theta, z, t) = (u, v, w)(r, \theta + \alpha, z, t), \quad (2a)$$

$$K_z(u, v, w)(r, \theta, z, t) = (u, v, -w)(r, \theta, -z, t), \quad (2b)$$

$$\phi_{t_0}(u, v, w)(r, \theta, z, t) = (u, v, w)(r, \theta, z, t + t_0). \quad (2c)$$

## A. Numerical methods

The Navier-Stokes equations (1) are solved using a second-order time-splitting method with consistent boundary conditions for the pressure [26,27]. Spatial discretization is via a Galerkin-Fourier expansion in  $\theta$  and Chebyshev collocation in  $r$  and  $z$ . The idealized boundary conditions are discontinuous at the junctions where the stationary end walls meet the rotating cylinders. In experiments there are small but finite gaps at these junctions where the azimuthal velocity adjusts to zero. For accurate use of spectral techniques, a regularization of the discontinuous idealized boundary conditions is implemented of the form

$$v(r, \theta, \pm 0.5\Gamma, t) = Re_i \exp([r_i - r]/\epsilon) + Re_o \exp([r - r_o]/\epsilon), \quad (3)$$

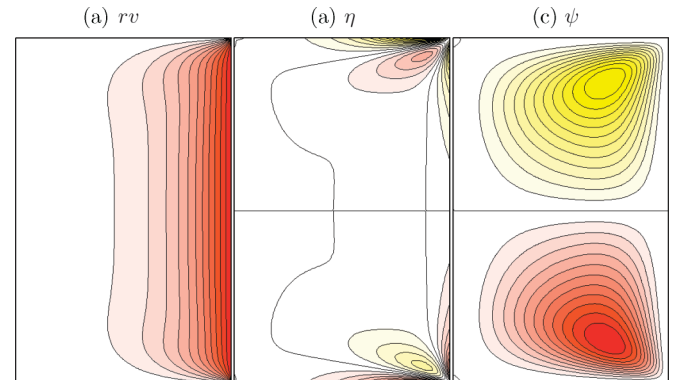


FIG. 1. (Color online) Contours of (a)  $rv$ , (b)  $\eta$ , and (c)  $\psi$  of  $f$  at  $Re_i = 0$ . Red (dark gray) and yellow (light gray) correspond to positive and negative values, respectively, with zero being white. The left (right) border is the inner (outer) cylinder. There are 12 positive and negative contours with  $rv \in [-800, 800]$ ,  $\eta \in [-1400, 1400]$ , and  $\psi \in [-2, 2]$ .

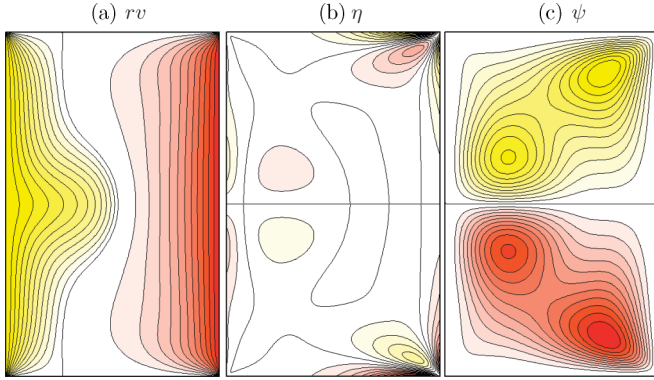


FIG. 2. (Color online) Contours of (a)  $rv$ , (b)  $\eta$ , and (c)  $\psi$  of  $f$  at  $Re_i = 150$ . The contour levels are the same as in Fig. 1.

where  $\epsilon$  is a small parameter that characterizes the physical gaps (see Ref. [28] for further details on the use of this type of regularization in spectral codes). In the solutions reported here, we have used  $\epsilon = 6 \times 10^{-3}$ . The numerical code has been previously used to study end wall effects in Taylor-Couette problems with corotating cylinders in short annuli [29,30]. Up to  $n_r = 50$  and  $n_z = 100$  Chebyshev modes in the radial and axial directions, up to  $n_\theta = 32$  Fourier modes in the azimuthal direction, and time steps  $\delta t = 0.001$  have been used.

### III. BASIC STATE

In this study we focus on the strongly counterrotating regime and as such we shall set  $Re_o = -500$  and increase  $Re_i$  from 0 to order  $-Re_o$ . Also, in contrast to most counterrotating studies, we shall focus on the short-annulus regime with  $\Gamma = 1.6$  and the wide-gap regime with  $R_i/R_o = 0.5$ . We consider the situation where the end walls are stationary and this has the effect of creating a region of nearly zero angular momentum separating the boundary layers on the two cylinders. Other conditions on the end walls can be expected to have significant influences on the dynamics, as had been observed in the Taylor-Couette flow with a rotating inner cylinder, a stationary outer cylinder, and one end wall stationary and the other

corotating with the inner cylinder [31,32]. In the present study we consider only the stationary end wall case.

The steady (fixed point) basic state  $f$  is axisymmetric and reflection symmetric about the midplane, i.e.,  $SO(2) \times Z_2 \times \mathbb{R}$  equivariant. When the inner cylinder is stationary  $Re_i = 0$ , the angular momentum  $rv$  diffuses into the interior from the rotating outer cylinder. For an infinitely long annulus, there would be no meridional flow; however, the presence of stationary end walls means that the vortex lines (isolines of angular momentum for axisymmetric flows) must bend away from the axial direction to become tangential to the stationary end walls [33,34]. In doing so, all vortex lines emerge from and terminate at the small gaps where the rotating outer cylinder meets the stationary top and bottom end walls. This vortex line bending into the corners produces corner jet flows that lead to meridional circulations of opposite senses in the top and bottom halves of the annular gap. The jet structures are best seen in the contours of the azimuthal vorticity  $\eta$  and the corresponding meridional circulations are seen in terms of the streamlines  $\psi$ , where  $(\partial_z^2 + \partial_r^2 - 1/r\partial_r)\psi = -r\eta$ . Figure 1 shows contour plots of  $rv$ ,  $\eta$ , and  $\psi$  for this state.

As  $Re_i$  is increased from zero, an angular momentum boundary layer forms on the inner cylinder and for sufficiently small  $Re_i$  angular momentum diffuses radially into the interior, except again near the junctions of the stationary top and bottom end walls with the rotating inner cylinder. As was the case with the vortex lines near the outer cylinder, the vortex lines associated with the inner cylinder boundary layer are also all bent into the top and bottom junction gaps, but here the vortex line bending leads to meridional flows into the inner cylinder junctions. This meridional circulation flows in the inner cylinder boundary layer from the end walls toward the midplane where the two streams meet and form a jet of angular momentum that is directed radially outward. This results in a slight squeezing of the outer cylinder boundary layer flow. The basic state  $f$  at  $Re_i = 150$  shown in Fig. 2 can be compared with  $f$  at  $Re_i = 0$  in Fig. 1. The jet emanating from the inner cylinder develops smoothly with increasing  $Re_i$ , but strengthens noticeably for  $Re_i$  beyond about 140. Apart from viscous diffusion of angular momentum and the vortex bending mechanism described above, as  $Re_i$  is

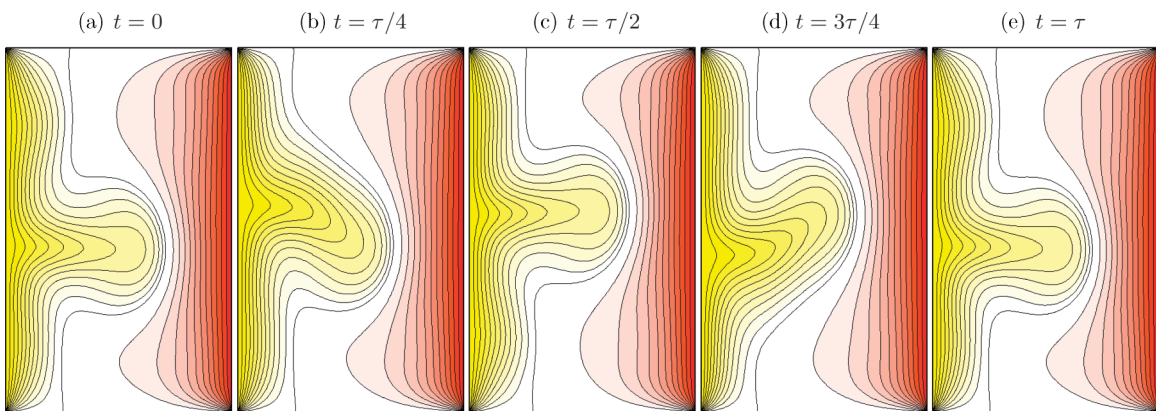


FIG. 3. (Color online) Contours of  $rv$  for  $l$  at  $Re_i = 300$  over one period  $\tau \approx 0.137$  at indicated times. There are 12 positive and negative contours with  $rv \in [-870, 870]$ ; red (dark gray) and yellow (light gray) correspond to positive and negative values, respectively, with zero being white (see Ref. [35(a)]).

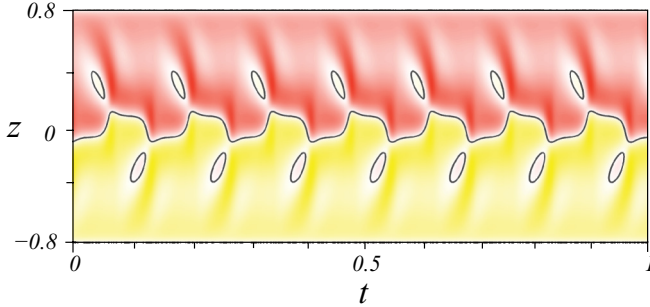


FIG. 4. (Color online) Space-time plot of  $\eta$  on the inner cylinder for  $l$  at  $Re_i = 300$ . Red (dark gray) and yellow (light gray) correspond to positive and negative values, with  $\eta \in [-1050, 1050]$ .

increased, the radial profile of angular momentum near the inner cylinder is centrifugally unstable and at large enough  $Re_i$  this leads to an advection-dominated redistribution of angular momentum. This is analogous to the situation with natural convection where there is a smooth transition from conduction dominated to convection-dominated heat transport rather than a bifurcation from a conduction state to a convection state as in classical Rayleigh-Bénard convection.

#### IV. HOPF BIFURCATION OF THE BASIC STATE

As  $Re_i$  is increased beyond about 257.6, the basic state  $f$  loses stability via a supercritical symmetry-breaking Hopf bifurcation  $H_1$ . The bifurcating limit cycle  $l$  remains axisymmetric, but the midplane reflection symmetry is broken. However, this broken spatial  $K_z$  symmetry is replaced by a spatiotemporal symmetry  $\mathcal{S}$  consisting of the midplane reflection  $K_z$  composed with a half-period time evolution. The physical manifestation of this is evident in the jet that in the basic state emanates symmetrically at the midplane now emanating from an axial location that oscillates about the midplane. When the point of emission is in the upper (lower) half, the jet is directed downward (upward). Figure 3 shows

five snapshots of the angular momentum  $rv$  over one period  $\tau$  illustrating the jet dynamics (an animation is available in Ref. [35(a)]). The figure also illustrates the half-period-flip symmetry  $\mathcal{S}$ , whereby  $K_z(l(t)) = l(t + \tau/2)$ . The action of  $\mathcal{S}$  on the velocity field is

$$\mathcal{S}(u, v, w)(r, \theta, z, t) = (u, v, -w)(r, \theta, -z, t + \tau/2) \quad (4)$$

and we can formally write  $\mathcal{S} = K_z\phi_{\tau/2}$  [see Eq. (2)]. Acting on a  $\tau$ -periodic solution,  $\mathcal{S}^2 = I$  is the identity and so the complete symmetry group of  $l$  is  $SO(2) \times Z_2^{\text{st}}$ , where the first factor consists of the purely spatial symmetries, while the second factor corresponds to the spatiotemporal symmetry group generated by  $\mathcal{S}$ .

Figure 4 provides another perspective of the half-period-flip symmetry of  $l$ . It shows a space-time diagram of the azimuthal vorticity on the inner cylinder wall  $\eta(r_i, 0, z, t)$ . The zero contour level is in black and indicates where the two streams in the inner cylinder boundary layer meet near the midplane to separate into the outward jet. The circular regions of zero  $\eta$  are indicative of nascent secondary separations.

As global measures of the flow we use the modal kinetic energies

$$E_m = \int_0^{2\pi} \int_{-\Gamma/2}^{\Gamma/2} \int_{r_i}^{r_o} \mathbf{u}_m \mathbf{u}_m^* r dr dz d\theta, \quad (5)$$

where  $\mathbf{u}_m$  is the  $m$ th Fourier mode of the velocity field. For the axisymmetric limit cycle  $l$ , only  $E_0$  is nonzero. For local measures we use the azimuthal vorticity on the inner cylinder at two points symmetrically displaced about the midplane,  $\eta_{\pm} = \eta(r_i, 0, \pm\Gamma/4, t)$ . Figure 5 shows time series of  $E_0$  and  $\eta_{\pm}$  and the corresponding power spectral densities (PSDs) for  $l$  at  $Re_i = 300$ . Note that  $\tau$  is twice the period of the time series of  $E_0$ ; this is because  $l$  is half-period-flip invariant and so  $E_0(l(t)) = E_0(l(t + \tau/2))$ , whereas  $l$  is  $\tau$  periodic,  $l(t) = l(t + \tau)$ .

Figure 6 shows the variation with  $Re_i$  of the peak-to-peak amplitude of  $E_0$ ,  $\Delta E_0$ , along with the corresponding period of oscillation  $\tau$ . Near the  $H_1$  bifurcation at  $Re_i \approx 257.6$ ,  $\Delta E_0$

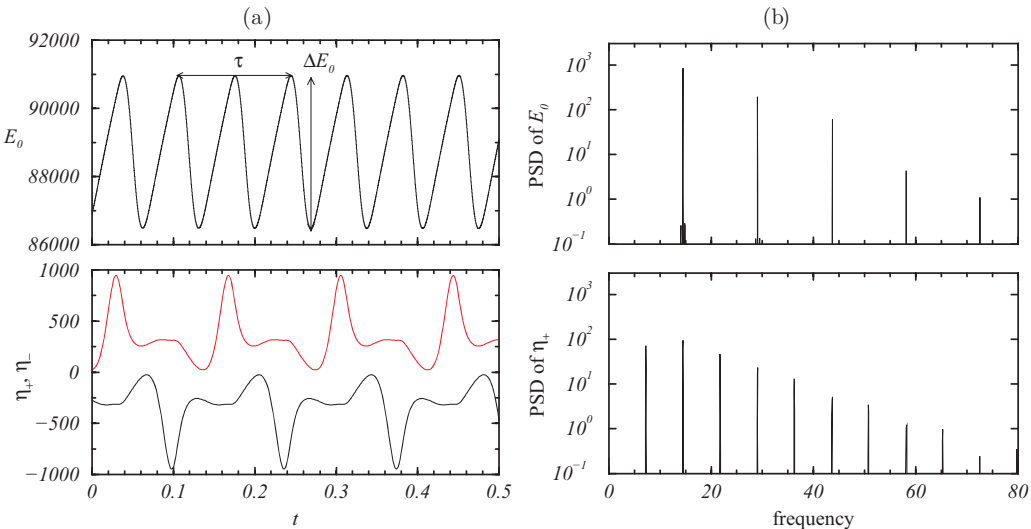
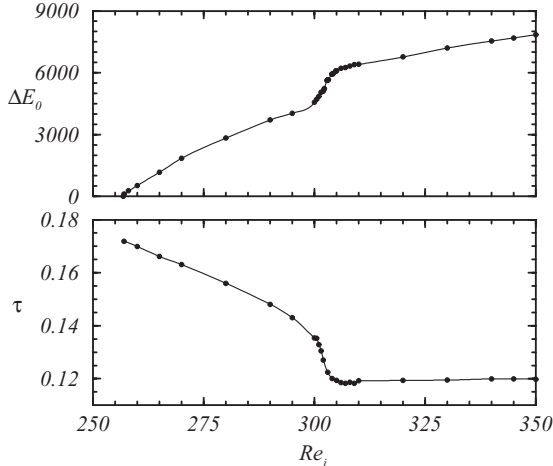


FIG. 5. (Color online) (a) Time series of  $E_0$ ,  $\eta_+$  [red (gray)], and  $\eta_-$  (black), and (b) the corresponding power spectral densities (PSD) for  $l$  at  $Re_i = 300$ .

FIG. 6. Variation of  $\Delta E_0$  and  $\tau$  with  $Re_i$  for  $l$ .

grows almost linearly and  $\tau$  decreases weakly with  $Re_i$ , which is typical of a supercritical Hopf bifurcation. At about  $Re_i = 300$ , there is a sudden change in how  $\Delta E_0$  and  $\tau$  vary with  $Re_i$ . This change is due to a smooth transition from a single jet emanating from the inner cylinder to having a second weaker jet emanating from the inner cylinder. This secondary jet is evident in Fig. 7, showing the angular momentum of  $l$  at  $Re_i = 320$ ; it is qualitatively similar to Fig. 3 corresponding to  $Re_i = 300$ , except that the secondary jet is very prominent. When this dynamic is established, by about  $Re_i = 310$ , the period of  $l$  shows virtually no variation with  $Re_i$  while the amplitude continues to rise.

The secondary jets appear alternately near the upper and lower end walls and merge with the central jet every half period. Their footprints are evident in the corresponding space-time plot of  $\eta$  on the inner cylinder shown in Fig. 8. Although secondary jets are not evident in the angular momentum contours at  $Re_i = 320$  (Fig. 7), their nascent presence is evident in the  $\eta$  space-time plot (Fig. 4). The emergence of the secondary jets and the ensuing dynamical complexity can be interpreted as a competition between different axial length scales being preferred for the centrifugal instability of the inner

cylinder boundary layer as  $Re_i$  is increased due to the short finite axial extent of the annulus.

## V. SO(2) SYMMETRY-BREAKING HOPF BIFURCATIONS

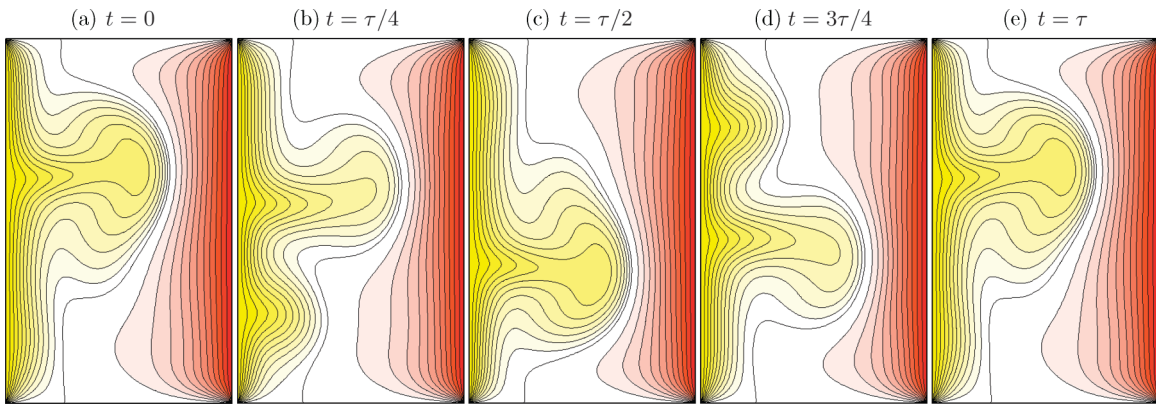
### A. Normal form of the Hopf bifurcation for maps with symmetry

Normal form theory provides useful insights on the symmetries and dynamical properties of bifurcated solutions, so in this section we discuss the normal form of a Hopf bifurcation from a limit cycle  $l$  with  $SO(2) \times Z_2^{\text{st}}$  symmetry group. The usual way to analyze the stability and bifurcations of periodic solutions is via a Poincaré map. Figure 9 shows a schematic of the Poincaré map corresponding to the periodic orbit  $l$  ( $T_1$ ). We select a convenient hyperplane  $\Pi$  transversal to  $l$  and starting with  $x(0) \in \Pi$  as the initial condition, we evolve in time until the trajectory intersects  $\Pi$  again; this is the Poincaré map  $\mathcal{P}$ . It is convenient that the Poincaré section  $\Pi$  be  $SO(2)$  symmetric:  $R_\alpha \Pi = \Pi \forall \alpha$ . We can visualize the action of  $R_\alpha$  on the phase of a solution  $x(t)$  as a rotation on the  $\Pi$  plane around  $\hat{T}_0$ , the intersection of  $l$  with  $\Pi$ . The space-time symmetry  $S = K_z \phi_{\tau/2}$  is also a map from  $\Pi$  to  $\Pi$ , as shown in the figure. Here  $\hat{T}_0 = T_1 \cap \Pi$  is a fixed point of both  $\mathcal{P}$  and  $S$ , indicating the half-period-flip symmetry of  $l$ .

The Poincaré map  $\mathcal{P}$  is the square of  $S$  and this may impose some constraints on  $\mathcal{P} = S^2$ . It is better to first determine the normal form for  $S$  and then from that obtain the corresponding normal form for  $\mathcal{P}$  [36]. The map  $S$  is  $SO(2)$  equivariant and we want to obtain the normal form corresponding to a bifurcation that breaks the  $SO(2)$  symmetry. Let  $A$  be the complex amplitude of the bifurcating eigenvector; the action of  $R_\alpha \in SO(2)$  on the eigenvector is of the form

$$R_\alpha(A, \bar{A}) = (e^{im\alpha} A, e^{-im\alpha} \bar{A}), \quad (6)$$

where  $\bar{A}$  is the complex conjugate of  $A$ . Here  $(A, \bar{A})$ , or their modulus and phase  $A = \rho e^{i\varphi}$ , will be used as coordinates of the center manifold of the bifurcation. The integer  $m$  characterizes the remaining symmetries of the bifurcated solution: It is invariant under the cyclic group of order  $m$ , termed  $Z_m$  or  $C_m$  in the literature, consisting of discrete rotations by multiples of  $2\pi/m$ . In our problem,  $m = 1$ .

FIG. 7. (Color online) Contours of  $rv$  of  $l$  at  $Re_i = 320$  over one period  $\tau \approx 0.119$  at indicated times. There are 12 positive and negative contours with  $rv \in [-891, 891]$ ; red (dark gray) and yellow (light gray) correspond to positive and negative values, respectively, with zero being white (see Ref. [35(b)]).

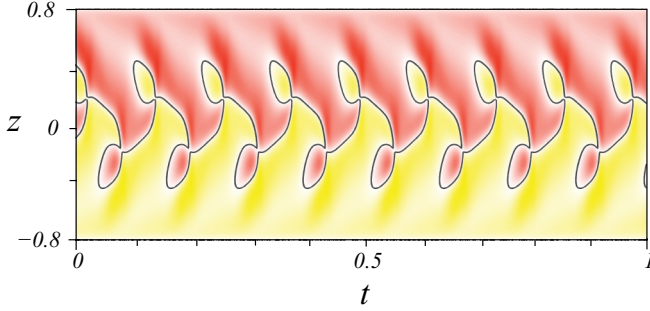


FIG. 8. (Color online) Space-time plot of  $\eta$  at the inner cylinder for  $t$  at  $\text{Re}_i = 320$ . Red (dark gray) and yellow (light gray) correspond to positive and negative values, with  $\eta \in [-1320, 1320]$ .

As the time evolution (the map  $\mathcal{S}$ ) commutes with the symmetry group, the action of  $L_{\mathcal{S}}$ , the linearization of the map  $\mathcal{S}$ , is of the form  $L_{\mathcal{S}}A = \lambda A$ . At the bifurcation point  $|\lambda| = 1$  and we finally arrive at

$$L_{\mathcal{S}}(A, \bar{A}) = (e^{i\beta} A, e^{-i\beta} \bar{A}), \quad (7)$$

where  $\beta$ , the phase of the  $\mathcal{S}$  eigenvalue, introduces a new frequency. The action of  $L_{\mathcal{S}}$  is exactly the same as the action of the rotation  $R_{\beta/2m}$ . The normal form for  $\mathcal{S}$ , up to order  $k$ , is of the form

$$\mathcal{S} : A \rightarrow e^{i\beta} A + P(A, \bar{A}) + o(|A|^k), \quad (8)$$

where  $P$  is a polynomial of order  $k$  that satisfies

$$\begin{aligned} P(e^{im\alpha} A, e^{-im\alpha} \bar{A}) &= e^{im\alpha} P(A, \bar{A}) \forall \alpha, \\ P(e^{i\beta} A, e^{-i\beta} \bar{A}) &= e^{i\beta} P(A, \bar{A}). \end{aligned} \quad (9)$$

As a result, the polynomial in two variables  $P$  collapses to a polynomial  $Q$  in one variable  $P(A, \bar{A}) = A Q(|A|^2)$ , as in the standard Hopf bifurcation. Up to third order in  $A$ , the normal form for  $\mathcal{S}$  is

$$\mathcal{S} : A \rightarrow A e^{i\beta} (1 + \sigma - c |A|^2), \quad \sigma, c \in \mathbb{C}, \quad (10)$$

where we have introduced the small parameter  $\sigma$ , which is zero at the bifurcation point, and  $c(\sigma = 0) \neq 0$  (the nondegeneracy condition). It is more convenient to write the normal form in terms of the modulus and phase of the amplitude  $A = \rho e^{i\varphi}$  and introduce real parameters  $\sigma = \mu + i\nu$  and  $c = a + ib$ . With

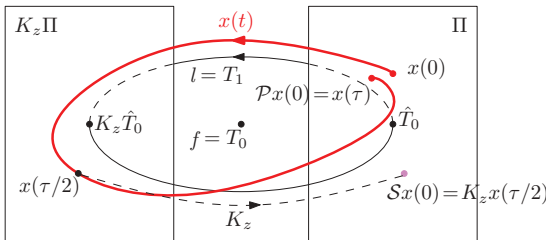


FIG. 9. (Color online) Schematics of the Poincaré map  $\mathcal{P}$  and half-period-flip map  $\mathcal{S}$ .

this, the normal forms for  $\mathcal{S}$  and  $\mathcal{P}$  are

$$\begin{aligned} \mathcal{S} : &\begin{cases} \rho \rightarrow \rho(1 + \mu - a\rho^2) \\ \varphi \rightarrow \varphi + \beta + v - b\rho^2, \end{cases} \\ \mathcal{P} : &\begin{cases} \rho \rightarrow \rho(1 + 2\mu - 2a\rho^2) \\ \varphi \rightarrow \varphi + 2\beta + 2v - 2b\rho^2. \end{cases} \end{aligned} \quad (11)$$

This is formally a codimension-2 bifurcation with two bifurcation parameters  $\mu$  and  $v$ . However, the amplitude dynamics is decoupled from the phase dynamics. Looking at the amplitude dynamics, it is a codimension-1 bifurcation with the same normal form as the Neimark-Sacker bifurcation. Assuming  $a > 0$  (the supercritical case), we have a fixed point  $\rho = 0$  that is stable for  $\mu < 0$ , loses stability at  $\mu = 0$ , and spawns a stable invariant circle  $\rho_0 = \sqrt{\mu/a}$  for  $\mu > 0$ ; the appearance of the invariant circle is a codimension-1 phenomenon. The dynamics on the invariant circle is very simple: a rotation of angle  $\varphi_0 = \beta + \delta$  every iteration of the half-period-flip map  $\mathcal{S}$  and of  $2\varphi_0$  for the Poincaré map  $\mathcal{P}$ . We have introduced the small drift  $\delta = v - b\rho_0^2 = v - b\mu/a$ , which is zero at the bifurcation point  $\mu = v = 0$ . The dynamics on the invariant circle is either periodic or quasiperiodic, depending on whether  $\varphi_0/\pi$  is rational or irrational. Therefore, the details of the phase dynamics depend on the value of the second parameter  $v$  and are therefore codimension-2 phenomena. This is a well-known result in dynamical system theory, described in detail in many textbooks [37,38]. The action of the symmetries on a bifurcated solution belonging to the invariant circle  $A_0(\varphi) = \sqrt{\mu/a} e^{i\varphi}$  is given by

$$R_\alpha : \varphi \rightarrow \varphi + m\alpha, \quad \mathcal{S} : \varphi \rightarrow \varphi + \beta + \delta = \varphi + \varphi_0. \quad (12)$$

From these equations we can draw some important conclusions. The actions of  $R_\alpha$  on the phase of the bifurcated solutions ( $\varphi \rightarrow \varphi + m\alpha$ ) and on the physical angle  $\theta$  in cylindrical coordinates [Eq. (2b)] ( $\theta \rightarrow \theta + \alpha$ ) are proportional. Moreover, the invariant circle is an SO(2) orbit: Starting with a point on the invariant circle and applying SO(2) to it, we obtain the whole invariant circle. Finally, the action of  $\mathcal{S}$  (or  $\mathcal{P}$ ) is the same as the action of a rotation of angle  $\alpha = \varphi_0/m$  ( $\alpha = 2\varphi_0/m$ ). On the bifurcated solutions, the action of  $\mathcal{S}$  is the same as the action of a rotation:  $\mathcal{S} = R_{\varphi_0/m}$ . Applying the Poincaré map (i.e., advancing in time one period) is also equivalent to a rotation of  $2\varphi_0/m$  of the phase solution  $\mathcal{P} = R_{2\varphi_0/m}$  or a physical rotation of  $2\varphi_0$  of the velocity field. Figure 10 illustrate these results. The invariant circle is  $\hat{T}_1^s$  and the dynamics of  $\mathcal{S}$  and  $\mathcal{P}$  is illustrated in Fig. 10(b):  $\gamma_1^s = \{x, \mathcal{P}x, \mathcal{P}^2x, \dots\}$  and  $\tilde{\gamma}_1^s = \{x, \mathcal{S}x, \mathcal{S}^2x, \dots\}$  are the discrete orbits generated by  $\mathcal{P}$  and  $\mathcal{S}$ , respectively. The small drift angle is also shown for the case  $\beta = \pi$ , which corresponds to the case in our fluid problem.

From the dynamics on the Poincaré section  $\Pi$  we can recover the dynamics in the whole phase space. Starting from  $x \in \hat{T}_1^s$  we can compute by time evolution the bifurcated quasiperiodic solution  $q_2^s$ ; the subindex 2 indicates that it is a quasiperiodic solution with two frequencies, one very close to the frequency of  $l$ ,  $\omega = 2\pi/\tau$ , and the other related to the dynamics on the invariant circle  $\hat{T}_1^s$ ,  $\omega_2 = \omega\varphi_0/\pi$ . The set of all quasiperiodic solutions constitutes the 2-torus  $T_2^s$ ; the curve  $q_2^s$  densely fills  $T_2^s$ , except when  $\varphi_0/\pi$  is rational, and the two frequencies  $\omega$  and  $\omega_2$  are in a rational ratio. The intersection of  $q_2^s$  with  $\Pi$  is the discrete orbit  $\gamma_1^s$ . We have seen that  $\mathcal{S} = R_{\varphi_0/m}$  on the bifurcating solution  $q_2^s$ . Therefore,  $q_2^s$  is invariant under

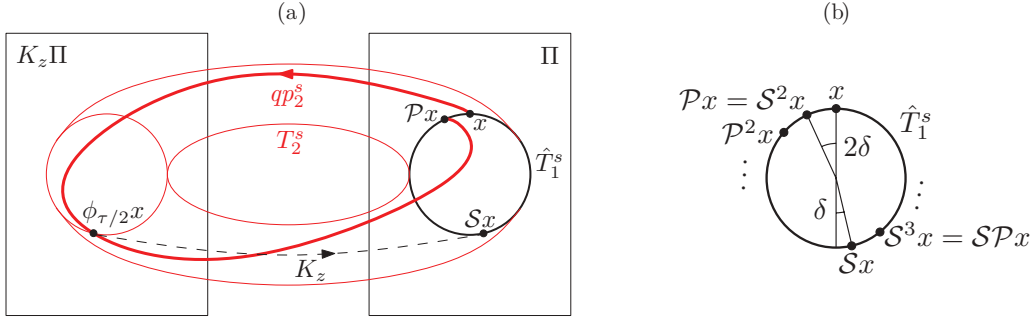


FIG. 10. (Color online) Schematics of the quasiperiodic solution  $q_2^s$  starting at  $x$  and the discrete orbits made of the iterates of  $\mathcal{P}$  and  $\mathcal{S}$  acting on  $x$ .

a new spatiotemporal symmetry  $\tilde{\mathcal{S}} = R_{-\varphi_0/m}\mathcal{S}$ ; the superindex  $s$  on  $q_2^s$  indicates the presence of this spatiotemporal symmetry. The square of  $\tilde{\mathcal{S}}$ ,  $\tilde{\mathcal{S}}^2 = R_{-2\varphi_0/m}$ , is a purely spatial symmetry that generates a cyclic subgroup of  $\text{SO}(2)$ , which is finite or numerable depending on whether  $\varphi_0/\pi$  is rational or irrational. Hence the spatial symmetry group  $G^s$  of the bifurcating solution is generated by the rotation  $R_{2\varphi_0/m}$  resulting from the breaking of  $\mathcal{S}$  and the rotations  $R_{2\pi/m}$  resulting from the breaking of  $\text{SO}(2)$ . The complete symmetry group of the bifurcating solution is obtained by adjoining  $\tilde{\mathcal{S}}$  to  $G^s$ , the details depending on the relationship between  $\beta$  and  $m$ . The symmetries of an individual solution  $q_2^s$  can be quite complicated. However, the symmetries of the set  $T_2^s$  are much simpler. The invariant circle  $\hat{T}_1^s$  does not change under arbitrary rotations. Also, the action of  $\mathcal{S}$  changes only the phase  $\varphi$  of the solution but not its modulus. Applying either a rotation  $R_\alpha$  or  $\mathcal{S}$  transforms one  $q_2^s$  solution to a different  $q_2^s$  solution, but both are in the same 2-torus  $T_2^s$ . Moreover,  $T_2^s$  is invariant under time evolution  $\phi_t$  (by definition, because it consists of all the  $q_2^s$  solutions). Since  $K_z = \mathcal{S}\phi_{\tau/2}$ , the 2-torus  $T_2^s$  is also  $K_z$  symmetric. The complete symmetry group of  $T_2^s$ , as a set, is  $\text{SO}(2) \times Z_2 \times \mathbb{R}$ , the symmetry group of the governing equations. The bifurcated solutions  $l$  and  $q_2^s$  lose symmetries at each bifurcation, but the associated invariant sets  $T_1$  and  $T_2^s$  have the same symmetries as the governing equations. These two different kinds of symmetry are called pointwise and setwise symmetries [39,40].

Two particular cases  $\beta = 0$  and  $\pi$  result in an eigenvalue 1 for the Poincaré map  $\mathcal{P}$ . In the absence of symmetries, this would result in a saddle node of maps, i.e., a saddle node of periodic orbits of the underlying partial differential equation problem. The symmetries alter this scenario. For the case  $\beta = 0$ , the invariant circle consists of a continuous family of fixed points along the straight line  $v = b\mu/a$  in parameter space for both  $\mathcal{S}$  and  $\mathcal{P}$ . Instead of a saddle node we have a pitchfork-of-revolution bifurcation, with the circle of fixed points being the orbit on any of the fixed points under the action of  $\text{SO}(2)$ . Away from the line  $v = b\mu/a$ , instead of fixed points the dynamics result in a small drift  $\delta$  along the orbit. This is the origin of the second frequency, which is always present even in the case with  $\beta = 0$ . This also occurs in other problems with similar symmetries [see, for example, Ref. [41] for the  $O(2)$  symmetry]. In the  $\beta = 0$  case  $\tilde{\mathcal{S}} = \mathcal{S}$  and the half-period-flip symmetry is preserved along the line  $v = b\mu/a$  and it is preserved except for the small drift for other parameter values.

The  $\beta = \pi$  case is different. It also has a pitchfork-of-revolution bifurcation along the straight line  $v = b\mu/a$  and the corresponding drift dynamics for other parameter values. However, in this case, the  $\mathcal{S}$  symmetry  $\mathcal{S} : \varphi \rightarrow \varphi + \pi + \delta$  is broken. Along the line  $v = b\mu/a$  the eigenvector changes sign every half period and the bifurcating solution is invariant to  $\tilde{\mathcal{S}} = R_{-\pi/m}\mathcal{S} = R_{-\pi/m}K_z\phi_{\tau/2}$ ; away from the line  $v = b\mu/a$  we have the same invariance plus a small drift. The new spatiotemporal symmetry  $\tilde{\mathcal{S}}$  consists of advancing half a period in time and applying a spatial symmetry consisting of a rotation of angle  $-\pi/m$  followed by the reflection  $K_z$ . This spatial symmetry is called an improper rotation (or rotoreflection, or rotary reflection) of angle  $-\pi/m$ . The improper rotation generates what is called in crystallography the  $S_{2m}$  Spiegel group; this group is illustrated in Fig. 11 for the  $m = 6$  case. The spatiotemporal group generated by  $\tilde{\mathcal{S}}$  is isomorphic with  $S_{2m}$ , but the odd powers of  $\tilde{\mathcal{S}}$  include a half-period advance in time, while the even powers of  $\tilde{\mathcal{S}}$  are purely spatial and coincide with the  $Z_m$  group generated by the rotation  $R_{2\pi/m}$ . A particularly simple case is  $m = 1$ , which is the case in our problem. In this case  $\tilde{\mathcal{S}} = R_\pi\mathcal{S} = R_\pi K_z\phi_{\tau/2} = \mathcal{I}\phi_{\tau/2}$ , where  $\mathcal{I}$  is the central inversion symmetry. Since  $\mathcal{I}^2 = I$  is the identity, the symmetry group of the bifurcated solution is  $\tilde{Z}_2^{\text{st}}$  generated by  $\tilde{\mathcal{S}}$  along the line  $v = b\mu/a$ . Away from this line the symmetry group is  $\langle \tilde{\mathcal{S}} \rangle$ , the cyclic group generated

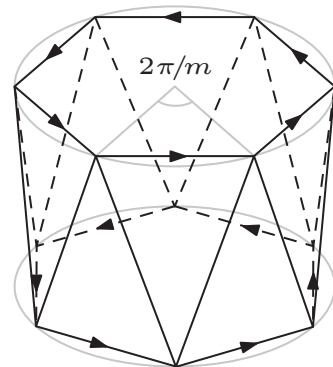


FIG. 11. Symmetries of the antiprism with  $m$  sides form the Spiegel group  $S_{2m}$ ; the  $m = 6$  case is shown. The symmetry group is generated by a rotation of  $\pi/m$  around the vertical axis followed by a midplane reflection. The top and bottom hexagons have been oriented with arrows in order to avoid reflection symmetries on vertical planes through the axis.

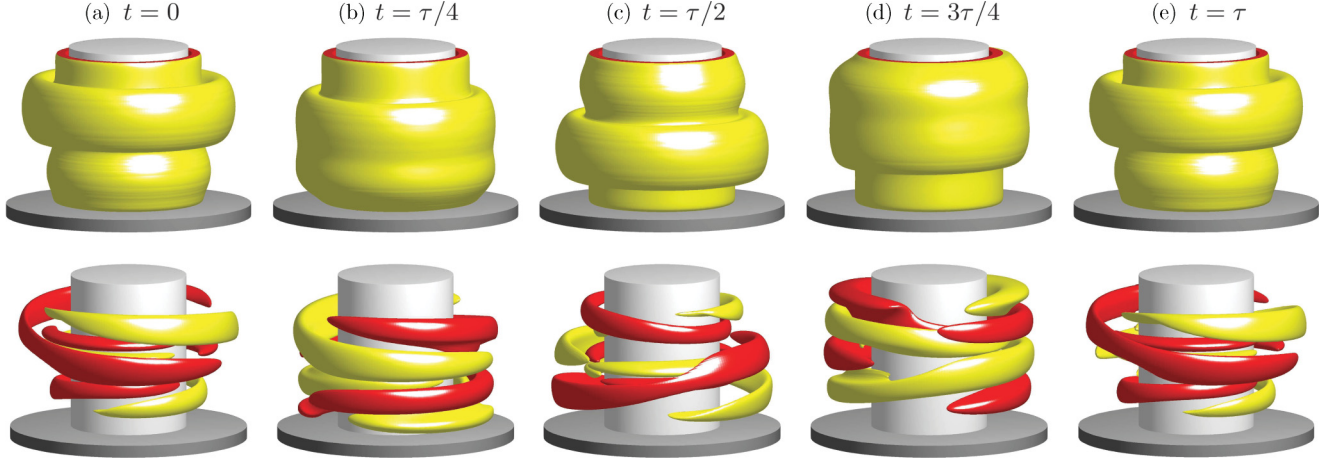


FIG. 12. (Color online) Isosurfaces of  $rv$  at indicated times  $t$  over one period ( $\tau \approx 0.118$ ) of  $q_2^s$  at  $Re_i = 365$ ; the top row is of the full solution (isolevel shown at  $rv = 100$ ) and the bottom row is of the  $m = 1$  contributions (isolevel shown at  $rv = \pm 10$ ) (see Ref. [35(c)]).

by  $\tilde{\mathcal{S}}$ , which can be finite (isomorphic to  $Z_q$  for some integer  $q$ ) or numerable (and then isomorphic to the additive group of integers  $\mathbb{Z}$ ), depending on  $\delta/\pi$  being rational or irrational.

The phase dynamics depends critically on the symmetry group. If the system were  $O(2)$  equivariant instead of  $SO(2)$  equivariant, then  $v = b = 0$  and the phase dynamics would be trivial. However, in the  $O(2)$  equivariant case the center manifold is four dimensional and there is the possibility of rotating waves in both directions  $\pm\theta$  as well as standing waves. With  $SO(2)$  symmetry the picture is simpler: There are only rotating waves in a given direction (specified by the sign of  $\beta$ ), but the precession angle  $\theta_0$  is not constant; it varies linearly with the bifurcation parameters  $\mu$  and  $v$ . This linear variation in precession angle is what we call a slow drift of the bifurcated solution along the invariant circle. Even in the special case  $\beta = 0$ , a new frequency appears due to the drift; however, in this case it is possible to fine-tune the bifurcation parameters in

order to suppress the drift along the line  $v = b\mu/a$  in parameter space. By fitting a straight line to the precession frequency as a function of the bifurcation parameter  $\mu$ , it is possible to determine both  $\beta$  and the ratio  $b/a$ .

### B. Two-torus state $q_2^s$

Increasing  $Re_i$ , the axisymmetric limit cycle  $l$  loses stability in an  $SO(2)$  symmetry-breaking Hopf bifurcation  $H_2$  at  $Re_i \approx 356.3$ . The bifurcating solution  $q_2^s$  is a quasiperiodic state with azimuthal wave number  $m = 1$ . It has one frequency  $\tau$  that corresponds to that of the underlying  $l$  from which it bifurcated and an additional frequency due to the Hopf bifurcation that corresponds to a counterclockwise (viewed from the top) mean precession of the  $m = 1$  spatial structure. This is precisely the situation that the normal form theory presented in the preceding section indicates. Due to this mean precession,  $q_2^s$  is not half-period-flip invariant, but it is still invariant to a new spatiotemporal symmetry (denoted  $\tilde{\mathcal{S}}$  in the preceding section) whose action consists of that of the half-period-flip symmetry composed with an additional rotation about the axis by a small drift angle  $\delta$ .

Figure 12 shows isosurfaces of  $rv$  for the full solution (top row) and the  $m = 1$  contribution (bottom row) of  $q_2^s$  at  $Re_i = 365$  at five times over one period of the underlying axisymmetric oscillation associated with the central jet ( $\tau =$

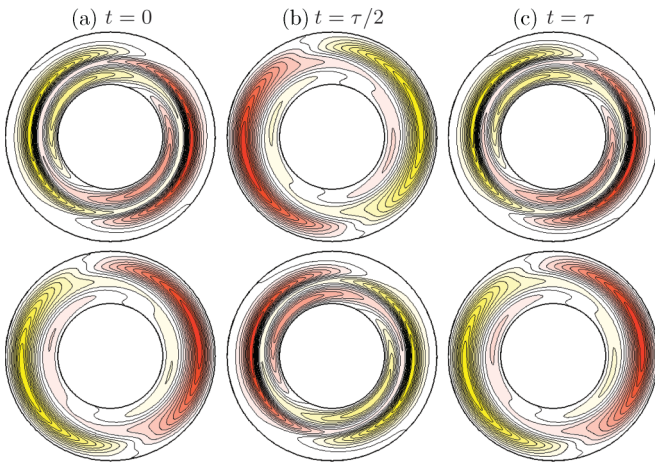


FIG. 13. (Color online) Contours of  $rv$  at indicated times over one period ( $\tau \approx 0.118$ ) for  $m = 1$  contributions of  $q_2^s$  at  $Re_i = 365$ ; the top row is at  $z = \Gamma/4$  and the bottom row is at  $z = -\Gamma/4$ . There are 12 positive and negative contours with  $rv \in [-20, 20]$  (see Ref. [35(d)] for  $z = \Gamma/4$ ).

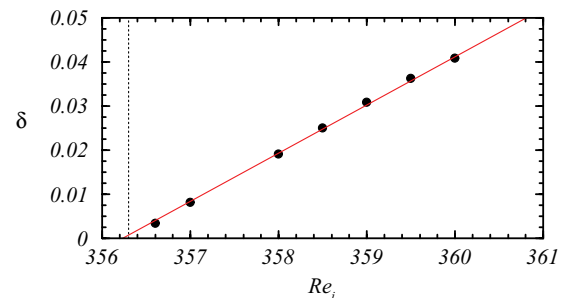


FIG. 14. (Color online) Variation of the drift angle  $\delta$  for  $q_2^s$  with  $Re_i$ . The red line is a linear fit and the vertical dotted line is the critical  $Re_i$  for  $H_2$ . The extrapolated value of  $\delta$  at  $H_2$  is 0.000 738.

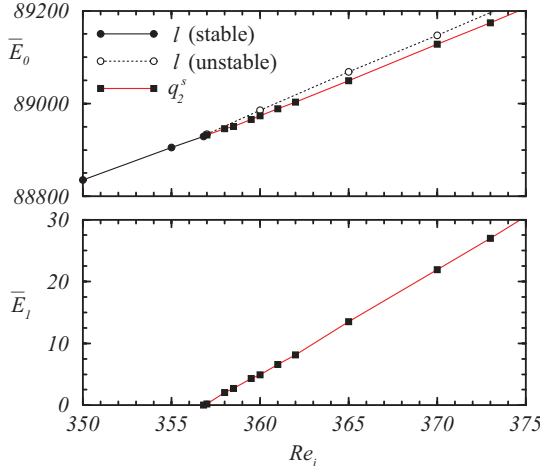


FIG. 15. (Color online) Variation with  $Re_i$  of  $\bar{E}_0$  and  $\bar{E}_1$  in the neighborhood of the Hopf bifurcation from  $l$  to  $q_2^s$ . The unstable  $l$  branch was found by restricting the computations to the axisymmetric subspace.

0.118). The flow is still dominated by the central jet oscillations about the midplane. As  $Re_i = 365$  is close to the critical value for  $H_2$ , the full  $q_2^s$  solution looks similar to  $l$ . However, plotting only the nonaxisymmetric components of  $r\nu$  reveals the  $m = 1$  contributions, which provide a very good approximation to the Hopf eigenfunction of  $r\nu$ . From Ref. [35(c)] it is apparent that the  $m = 1$  contributions correspond to a tilting of the secondary jets found in  $l$ . These appeared alternately above and below the midplane as the central jet oscillated up and down. In the  $q_2^s$  solutions these alternately appearing jets have an alternating sign of helix angle and sense of precession, but these are not perfectly symmetric due to the bias imposed by the rotation of the inner cylinder and so there is a net drift in azimuth, in accord with the normal form analysis of Sec. V A. By strobing the  $m = 1$  movie using a period of  $\tau$ , this drift becomes apparent as the strobed structure remains invariant except for a rotation given by the drift. Comparing the first and last frames of the second row of Fig. 12, one can see this

small drift, but it is much more clearly seen in Ref. [35(d)], which shows a strobed animation of the  $q_2^s$  over several periods. The strobed movie allows for a straightforward determination of the drift angle. Note that while the spiral structures rotate preferentially in the counterclockwise direction in continuous time, the drift is in the clockwise direction.

In order to determine the value of  $\beta$  (the critical eigenvalue of the  $S$  map) we must explore what happens with the half-period-flip map  $S$ . Comparing Figs. 12(a) and 12(c), we see that the eigenfunction (i.e., the second row in the figure) changes sign upon applying the half-period flip  $S$ , apart from a very small drift. Therefore, we have the  $\beta = \pi$  case. By plotting horizontal sections for two  $K_z$ -symmetric planes, at  $z = \pm\Gamma/4$  as illustrated in Fig. 13, we can precisely measure the drift angle  $\delta$ . According to the normal form theory, the variation of  $\delta$  with  $Re_i$  should be linear close to the bifurcation point. The variation of  $\delta$  with  $Re_i$  for  $q_2^s$  is shown in Fig. 14; indeed  $\delta$  varies linearly as predicted and it is very close to zero as  $Re_i$  approaches the bifurcation point  $H_2$ . This means that by slightly changing another parameter, such as the aspect ratio  $\Gamma$  or the rotation of the outer cylinder  $Re_o$  (which would play the role of  $\nu$  in the normal form theory), we can stop and even change the sign of the drift angle. Identifying the normal form parameter  $\mu$  with  $Re_i - Re_i^{\text{crit}}$ , the slope in Fig. 14 gives the value of  $b/a \approx 0.0109$ .

Since  $q_2^s$  is quasiperiodic,  $\Delta E_0$  is no longer a suitable global measure of the flow. Instead, we use as global measures the time-averaged kinetic modal energies  $\bar{E}_0$  and  $\bar{E}_1$  taken over a very long time (long enough so that the average does not change very much, typically several diffusion times). The bifurcation from  $l$ , spawning  $q_2^s$ , is shown in Fig. 15 in terms of both  $\bar{E}_0$  and  $\bar{E}_1$ , showing that it is a supercritical Hopf breaking  $SO(2)$  symmetry, with  $\bar{E}_1$  growing almost linearly from zero at the bifurcation and  $\bar{E}_0(q_2^s)$  deviating only slightly from that for the unstable  $l$  (which was found by restricting the computations to the axisymmetric subspace). The growth in  $\bar{E}_1$  with increasing  $Re_i$  is compensated for by a decrease in  $\bar{E}_0$ .

Figure 16 shows a phase portrait of  $q_2^s$  on  $(\eta_-, -\eta_+)$  at  $Re_i = 365$  and the corresponding two-dimensional Poincaré section

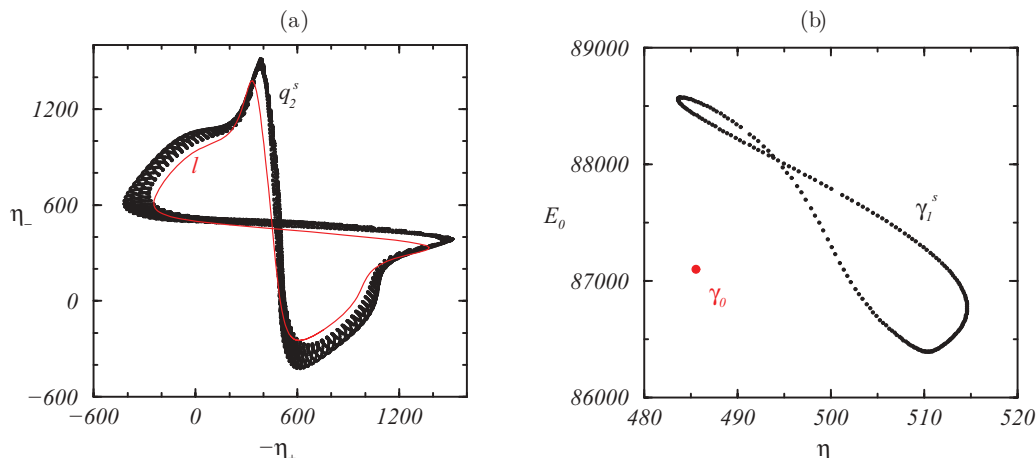
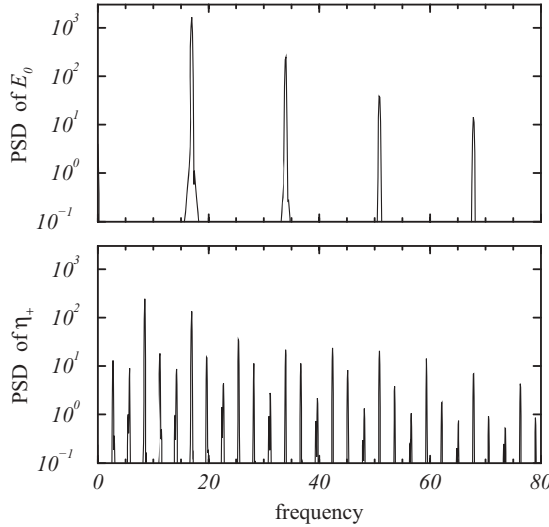
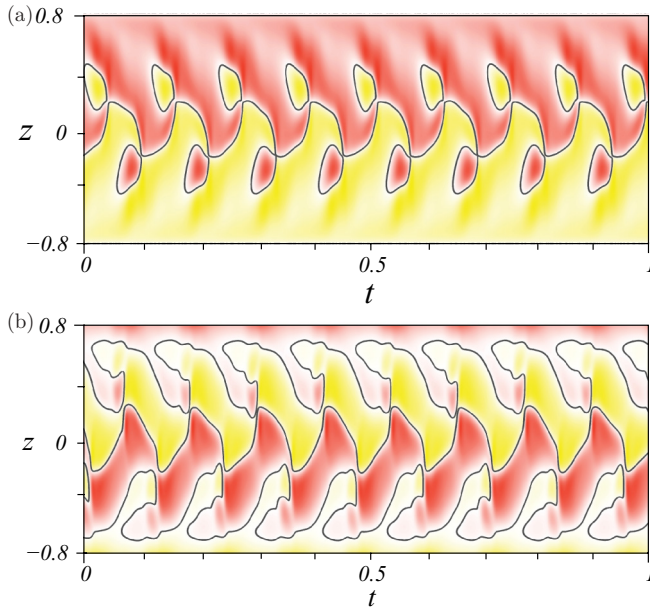


FIG. 16. (Color online) (a) Phase portraits of  $l$  ( $T_1$ ) at  $Re_i = 340$  and  $q_2^s$  ( $T_2^s$ ) at  $Re_i = 365$  on  $(\eta_-, -\eta_+)$  and (b) the corresponding two-dimensional Poincaré sections ( $E_0, \eta_-$ ) with  $\eta_+ = -200$ ;  $\gamma_0 = l \cap \Pi$  and  $\gamma_1^s = q_2^s \cap \Pi$ .

FIG. 17. Power spectral density of  $E_0$  and  $\eta_+$  for  $q_2^s$  at  $Re_i = 365$ .

for  $\eta_+$  on  $(E_0, \eta_-)$ . The Poincaré section used corresponds to  $\eta_+ = -200$ . For comparison, the red (gray) curve in the phase portrait corresponds to  $l$  at  $Re_i = 340$  whose corresponding Poincaré section is a single point. From the phase portrait it is clear that  $T_2^s$ , the 2-torus on which  $q_2^s$  resides, is setwise symmetric.

Figure 17 shows the PSD of  $E_0$  and  $\eta_+$  for a  $qp_2^s$  close to the Hopf bifurcation  $H_2$ . The PSD of  $E_0$  spectra for  $q_2^s$  is qualitatively the same as that for  $l$  (Fig. 5), consisting of  $\omega$  and its harmonics, whereas the  $\eta_+$  spectra for  $qp_2^s$  has an additional incommensurate frequency plus all the linear combinations. This new frequency is due to the Hopf bifurcation; it is very nearly 1/3 of the primary frequency of  $\eta_+$  ( $\omega$ ), the incommensurate nature being associated with the small drift

FIG. 18. (Color online) Space-time plot of  $\eta$  for  $q_2^s$  at (a) the inner cylinder and (b) the midgap at  $Re_i = 365$ . Red (dark gray) and yellow (light gray) correspond to positive and negative values, with (a)  $\eta \in [-1480, 1480]$  and (b)  $\eta \in [-750, 750]$ .

$\delta$ . None of this appears in the  $E_0$  spectra as it is associated with nonaxisymmetric dynamics, which simply correspond to precession and as such do not affect the global kinetic energy of the solution.

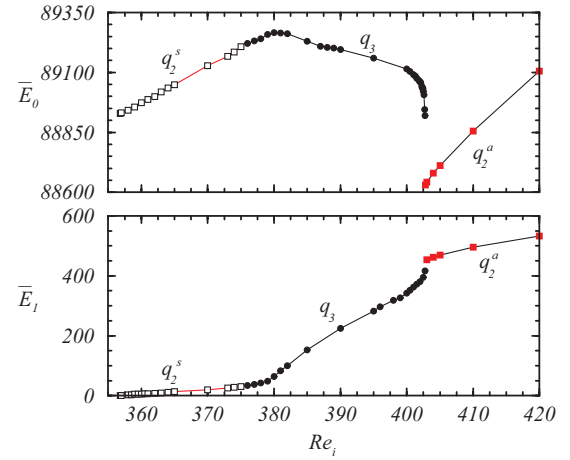
The additional frequency in  $q_2^s$  destroys the half-period-flip symmetry. This, however, is not readily appreciated in the space-time plot of  $\eta$  on the inner cylinder, shown in Fig. 18(a) for  $q_2^s$  at  $Re_i = 365$ ; it is very similar to that of  $l$  (Fig. 4), which is half-period-flip symmetric. In contrast, the space-time plot of  $\eta$  at midgap,  $r = (r_i + r_o)/2$ , shown in Fig. 18(b), does show the broken half-period-flip symmetry of  $q_2^s$ , indicating that the symmetry breaking is dominated by the dynamics of the jets in the bulk interior flow.

## VI. THREE-TORUS STATE $T_3$ AND ITS BREAKUP

Further increasing  $Re_i$ ,  $q_2^s$  becomes unstable at  $Re_i \approx 375.6$ , where a further frequency  $\omega_3$  appears and a new quasiperiodic solution  $q_3$  with three frequencies is found; this solution exists in a 3-torus invariant manifold  $T_3$ . Three-torus states are not commonly found in hydrodynamics. Often they are found in periodically forced systems [42–45], but have also been found in unforced flows [11,46–48], as is the case in the present problem. This is in line with the theoretical expectation of their occurrence in typical nonlinear dynamical systems [49].

Figure 19 shows the variations in  $\bar{E}_0$  and  $\bar{E}_1$  over a range of  $Re_i$  that includes the Hopf bifurcation  $H_2$  from  $l$  to  $q_2^s$ , described in the preceding section, and the Hopf bifurcation  $H_3$  from  $q_2^s$  to  $q_3$ . Near this bifurcation the mean modal energies of  $q_3$  vary with  $Re_i$  in a qualitatively similar fashion as they do for  $q_2^s$ , but for  $Re_i \gtrsim 380$ ,  $\bar{E}_1$  grows much more rapidly and as a consequence  $\bar{E}_0$  decreases with increasing  $Re_i$ .

By  $Re_i = 400$ , the flow dynamics of  $q_3$  are significantly different from those of  $q_2^s$ . Figure 20 shows isosurfaces of  $rv$  for the full solution and its  $m = 1$  contributions (bottom row) of  $q_3$  at five times over a period  $\tau = 0.196$  at  $Re_i = 400$ . While the flow dynamics continues to be dominated by the central jet oscillating up and down, much like with  $l$  and  $q_2^s$ , for  $q_3$  the central jet has developed a significant  $m = 1$  wobble, which is

FIG. 19. (Color online) Variation with  $Re_i$  of  $\bar{E}_0$  and  $\bar{E}_1$  in the neighborhoods of the Hopf bifurcation from  $q_2^s$  to  $q_3^s$  and the SNIC bifurcation.

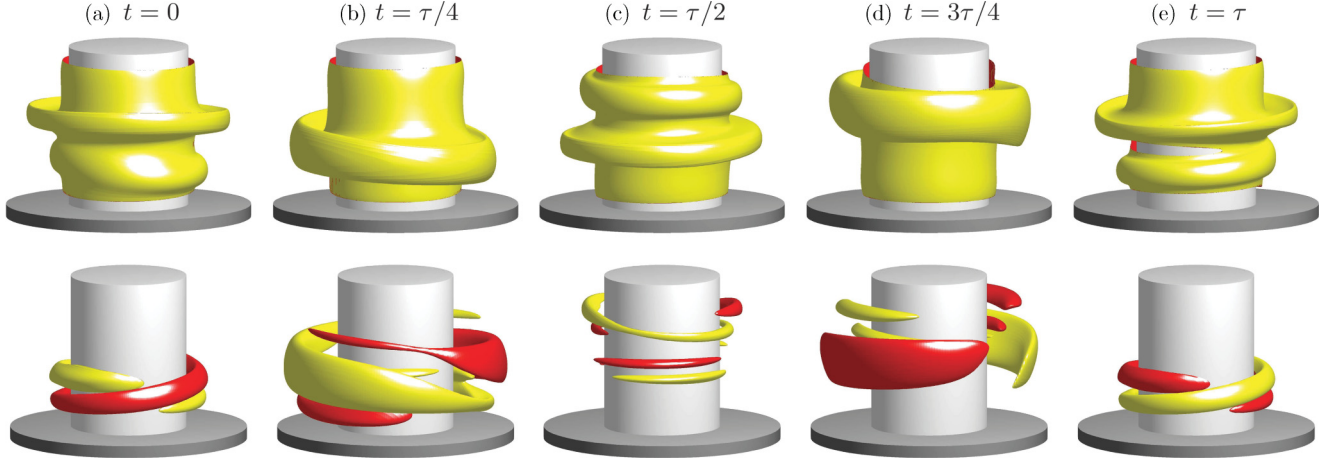


FIG. 20. (Color online) Isosurfaces of  $rv$  of the full solution (top row,  $rv = 300$ ) and of the  $m = 1$  contribution (bottom row,  $rv = \pm 45$ ) at five different times  $t$  as indicated over a time period  $\tau = 0.196$  for  $T_3$  at  $Re_i = 400$  (see Ref. [35(f)]).

clearly visible in the isosurface plots of the full solution. It is this wobble of the main central jet that contributes to the rapid growth in  $\bar{E}_1$  with  $Re_i$ . The emergence of the central jet and of the secondary jets from the inner cylinder boundary layer for  $q_3$  is very similar to that for  $q_2^s$ , as can be seen by comparing the space-time plot of  $\eta$  on the inner cylinder shown in Fig. 21(a) for  $q_3$  at  $Re_i = 400$  with that for  $q_2^s$  at  $Re_i = 365$  in Fig. 18. While the space-time plot of  $\eta$  on the inner cylinder suggests a half-period-flip symmetry, a space-time plot of  $\eta$  at midgap [Fig. 21(b)] clearly indicates that  $q_3$  has much more complicated dynamics. All the enhanced  $m = 1$  wobbling associated with  $q_3$  occurs in the interior, as suggested by the  $m = 1$  isosurfaces in the second row of Fig. 20.

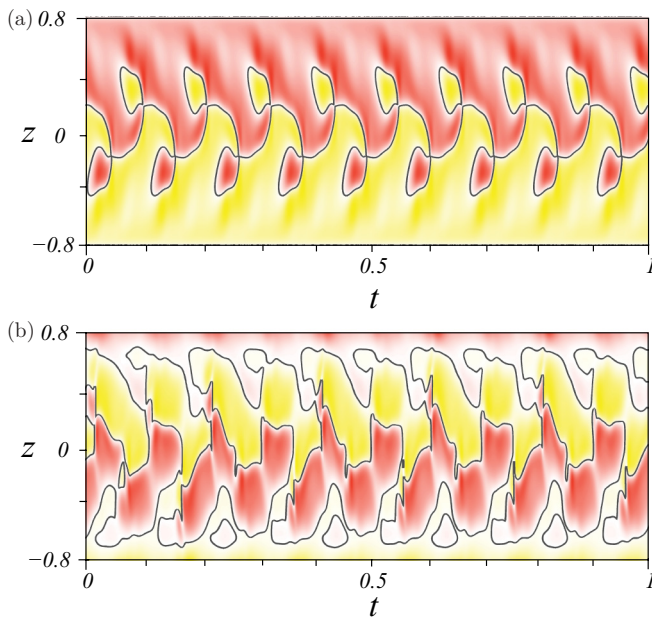


FIG. 21. (Color online) Space-time plot of  $\eta$  for  $q_3$  at (a) the inner cylinder and (b) the midgap at  $Re_i = 400$ . Red (dark gray) and yellow (light gray) correspond to positive and negative values, with (a)  $\eta \in [-1650, 1650]$  and (b)  $\eta \in [-860, 860]$ .

Figure 22 shows the PSD of  $E_0$ ,  $\eta_+$ , and  $\eta$  of  $q_3$  at  $Re_i = 400$ . The PSD of  $E_0$  does not contain the  $\omega_2$  frequency [which results from the azimuthal drift from having broken SO(2) symmetry] and so it consists only of  $\omega$  and the new frequency  $\omega_3$ , which emerges at the Hopf bifurcation  $H_3$ , and their linear combinations. In contrast, the PSD of  $\eta_+$  consists of linear combinations of all three frequencies. At  $Re_i = 400$  it is apparent that  $\omega_3$  is small compared to  $\omega$ .

The bifurcation from  $q_2^s$  to  $q_3$  can also be described by looking at the Poincaré section  $\Pi$ . Figure 23(a) shows a schematic of the invariant 2-torus  $\hat{T}_2^s$  that bifurcates in a secondary Neimark-Sacker bifurcation from the invariant circle  $\hat{T}_1^s$ . The schematic is on the Poincaré section  $\Pi$  (which is infinite dimensional) and can be compared with Fig. 10(b). By time evolution, starting from  $\hat{T}_2^s$  we obtain the 3-torus  $T_3$ . The solution of the Navier-Stokes equations starting from  $x$  generates a  $q_3$  curve that generically fills  $T_3$  densely. The intersection of  $q_3$  with  $\Pi$  results in the discrete orbit

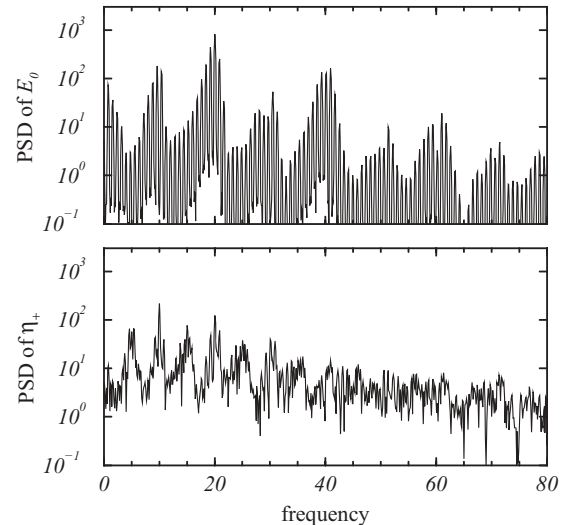


FIG. 22. Power spectral density of  $E_0$ ,  $\eta_+$ , and  $\eta$  for  $T_3$  at  $Re_i = 400$ .

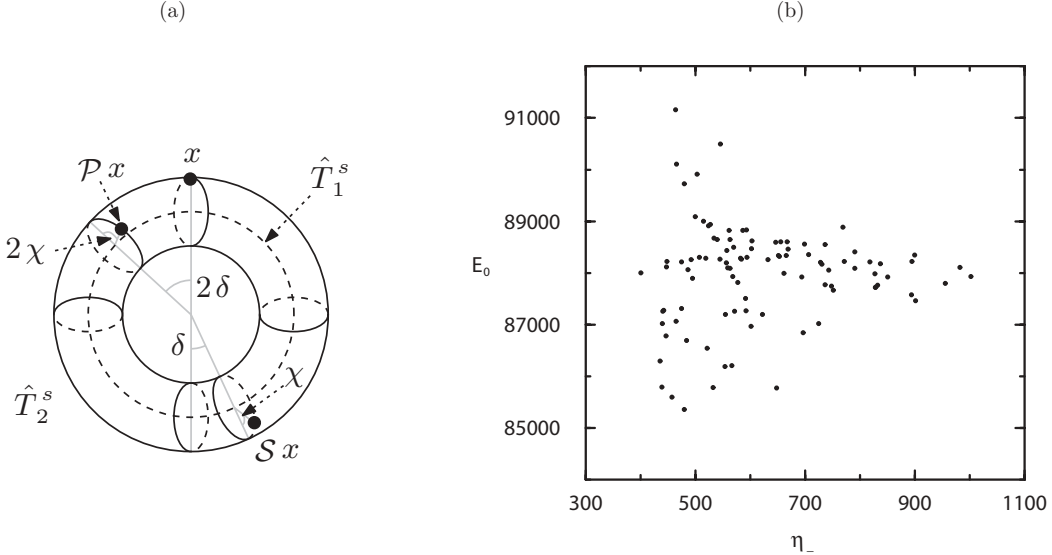


FIG. 23. (a) Schematic of the bifurcation from  $q_2^s$  to  $q_3$  viewed on the Poincaré section  $\Pi$ ; the invariant circle  $\hat{T}_1^s$  spawns  $\hat{T}_2^s$ . (b) Poincaré section ( $E_0, \eta_-$ ) with  $\eta_+ = -200$  of  $q_3$  at  $Re_i = 400$ .

generated by the Poincaré map  $\mathcal{P}$  acting on  $x$ :  $\gamma_2^s = q_2^s \cap \Pi = \{x, \mathcal{P}x, \mathcal{P}^2x, \dots\} \subset \hat{T}_2^s$ . The discrete orbit  $\bar{\gamma}_2^s$  generated by the half-period-flip map  $\mathcal{S}$  is  $\bar{\gamma}_2^s = \{x, \mathcal{S}x, \mathcal{S}^2x, \dots\}$ , which contains  $\gamma_2^s$  because  $\mathcal{S}^2 = \mathcal{P}$ :  $\gamma_2^s \subset \bar{\gamma}_2^s$ . Generically, both  $\gamma_2^s$  and  $\bar{\gamma}_2^s$  densely fill the invariant torus  $\hat{T}_2^s$ . The angle  $\chi$  is related to the third frequency of the quasiperiodic solution  $q_3$  in the usual way:  $\omega_3 = \omega\chi/\pi$ . Figure 23(b) shows a Poincaré section of  $q_3$  at  $Re_i = 400$ , using the same section as used for  $T_2^s$  earlier. As expected, it is clearly not a closed loop.

The characteristics of  $q_3$  change rapidly with  $Re_i$  for  $Re_i > 400$ . For  $Re_i \in (400, 403)$ , Fig. 19 shows that  $\bar{E}_1$  grows much more rapidly and  $\bar{E}_0$  decreases very rapidly with  $Re_i$ , corresponding to very large amplitude wobbles of the jets. At about  $Re_i = 402.8$ , the 3-torus ceases to exist as the frequency associated with the wobbles,  $\omega_3$ , goes to zero and the associated period becomes unbounded. Figure 24 shows a time series of  $E_0$  for  $q_3$  at various  $Re_i$ . For  $Re_i \gtrsim 400$  it has a

relaxation type of character typical of slow-fast dynamics and the long period associated with  $1/\omega_3$ , which we will now refer to as  $\tau_{\text{SNIC}}$ , is clearly evident.

The variation with  $Re_i$  of  $\tau_{\text{SNIC}}$  for  $q_3$  is shown in Fig. 25. As  $Re_i \rightarrow Re_{i,c} \approx 402.783$  from below,  $\tau_{\text{SNIC}} \rightarrow \infty$  following the  $1/\sqrt{Re_{i,c} - Re_i}$  scaling associated with the saddle-node-infinite-period (SNIC) bifurcation [38]. Open circles are the computed periods and the line gives a fit of the form  $\tau_{\text{SNIC}} = a_0 + a_1/\sqrt{Re_{i,c} - Re_i}$ .

In a classical SNIC, a saddle-node bifurcation takes place on an invariant cycle. Before the bifurcation the invariant cycle is a periodic solution and its period becomes unbounded as the bifurcation point is approached, following an inverse square-root law. At the bifurcation, a saddle and a node are created and are connected via two heteroclinic curves forming the invariant circle that ceases to exist after the bifurcation. Here the SNIC bifurcation takes place on a 3-torus state  $T_3$ ; the saddle and node are 2-torus states. Unlike  $T_2^s$ , which is  $K_z$  symmetric, the new 2-tori are not and so there is a pair of conjugate 2-tori, which we shall refer to as  $T_2^a$  and its conjugate as  $T_2^{*a}$  (obtained by applying the  $K_z$  reflection to  $T_2^a$ ).

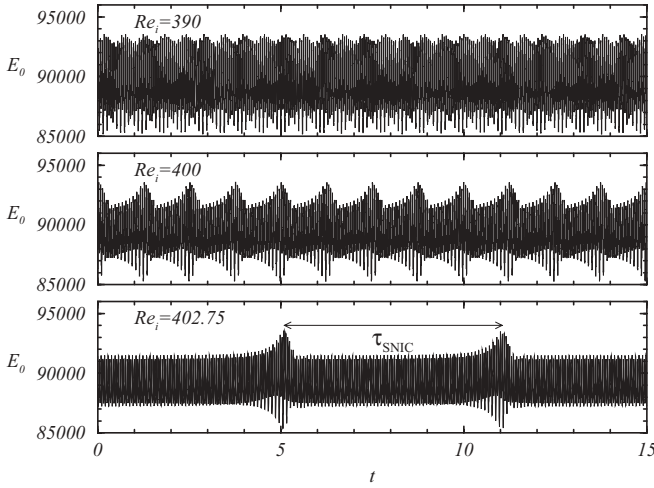


FIG. 24. Time series of  $E_0$  for  $T_3$  at  $Re_i$  as indicated.

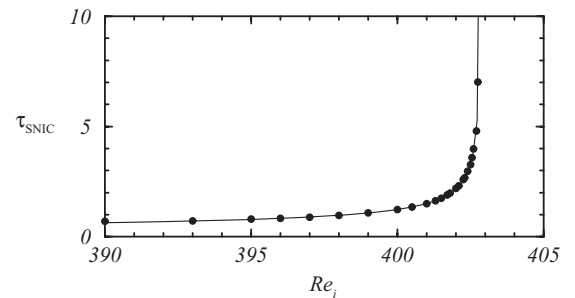


FIG. 25. Variation of  $\tau_{\text{SNIC}}$  with  $Re_i$  for  $T_3$ . The solid circles are the computed periods and the line is a fit of the form  $\tau_{\text{SNIC}} = a_0 + a_1/\sqrt{Re_{i,c} - Re_i}$ .

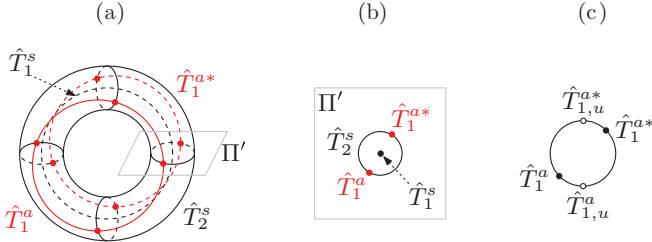


FIG. 26. (Color online) Schematics of the double SNIC bifurcation. (a) and (b) are at the SNIC bifurcation point, where the saddle nodes  $\hat{T}_1^a$  and  $\hat{T}_1^{a*}$  have just appeared. (c) is the situation after the SNIC bifurcation: The saddles (○) and nodes (●) separate. The unstable saddles  $\hat{T}_{1,u}^a$  and  $\hat{T}_{1,u}^{a*}$  cannot be observed.

Figure 26 shows a schematic of the double SNIC bifurcation on the invariant 2-torus  $\hat{T}_2^s$ , where a couple of  $K_z$ -asymmetric invariant circles  $\hat{T}_1^a$  and  $\hat{T}_1^{a*}$  bifurcate from the  $K_z$ -symmetric 2-torus  $\hat{T}_2^s$ . The asymmetric invariant circles are symmetrically related:  $\hat{T}_1^{a*} = K_z \hat{T}_1^a$ . The schematic is on the Poincaré section  $\Pi$ . Here  $\Pi'$  is a second Poincaré section made on  $\Pi$ , showing the relationships between  $\hat{T}_2^s$ ,  $\hat{T}_1^a$ ,  $\hat{T}_1^{a*}$ ,  $\hat{T}_1^a$ , and  $\hat{T}_2^s$ . The second Poincaré section  $\Pi'$  can be physically realized in a precessing system where the precession frequency of the different solutions disappears, so all the tori lose one dimension:  $\Pi$  becomes the whole phase space and  $\Pi'$  becomes an ordinary Poincaré section.

Figure 27 shows a phase portrait on  $(\eta_-, -\eta_+)$  and a corresponding two-dimensional Poincaré section for  $\eta_+$  on  $(E_0, \eta_-)$  of the 2-torus solution  $q_2^a$  at  $Re_i = 410$ . Compared to the phase portrait for  $q_2^s$  at lower  $Re_i$  in Fig. 16, it is more complicated, but still a 2-torus state as evidenced by the closed loop structure of the Poincaré section. The phase portrait [Fig. 27(a)] indicates that  $T_2^a$  is not symmetric. We have taken the  $q_2^a$  solution, reflected it, and used it as an initial condition for a time evolution and have obtained  $q_2^{a*}$ , whose phase portrait is the mirror image of Fig. 27(a) reflected about the line  $\eta_- = -\eta_+$ .

Figure 28 shows the corresponding power spectral density of  $E_0$  and  $\eta_+$  for  $q_2^a$  at  $Re_i = 410$ , following the SNIC; these

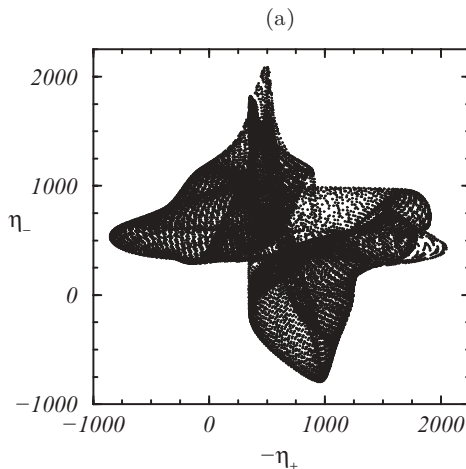


FIG. 27. (a) Phase portrait of  $q_2^a$  at  $Re_i = 410$  on  $(\eta_-, -\eta_+)$  and (b) the corresponding two-dimensional Poincaré section  $(E_0, \eta_-)$  with  $\eta_+ = -200$ .

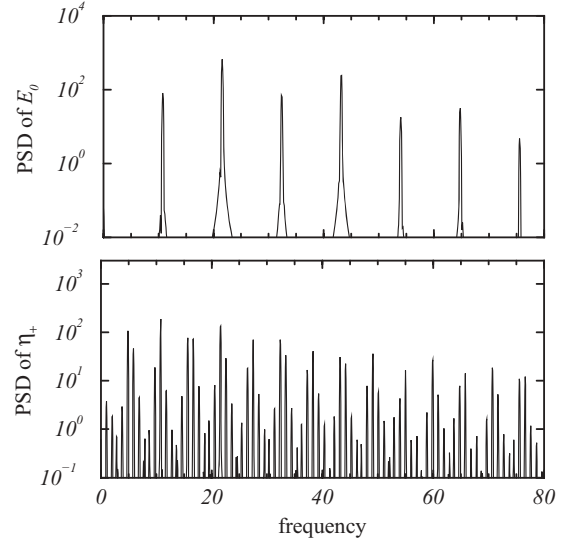
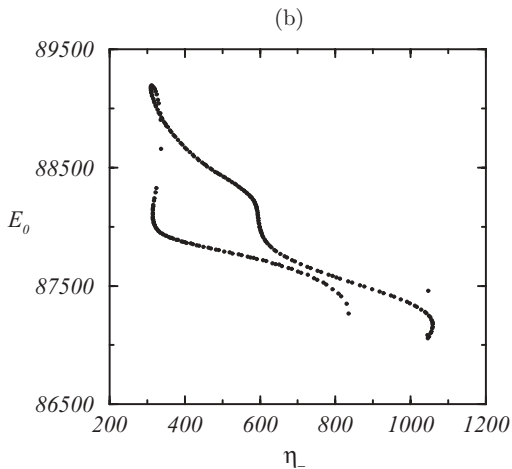


FIG. 28. Power spectral density of  $E_0$  and  $\eta_+$  for  $q_2^a$  at  $Re_i = 410$ .

are similar to the PSD for the  $q_2^s$  at lower  $Re_i$  (Fig. 17). Again, the PSD of  $E_0$  shows only the single frequency  $\omega$  and its harmonics and the PSD of  $\eta_+$  consists of linear combinations of  $\omega$  and  $\omega_2$ .

The flow dynamics of  $q_2^a$  are similar to those of  $q_3$ . Figure 29 shows  $rv$  isosurfaces of  $q_2^a$  for the full solution (top row) and its  $m = 1$  contributions (bottom row) at five times over a period  $\tau = 0.188$  at  $Re_i = 410$ . As for  $q_3$ , the flow dynamics is dominated by the central jet oscillating up and down interacting with the  $m = 1$  secondary jets. The  $m = 1$  wobble of the central jet is clearly visible in the isosurface plots of the full solution whereas, compared to Fig. 20, the secondary jets are less pronounced. However, the  $m = 1$  isosurfaces clearly illustrate the wobbling in the interior. The emergence of both central and secondary jets from the inner cylinder boundary layer remains very similar to that for  $q_3$ , as can be seen from space-time plot of  $\eta$  on the inner cylinder, whereas the space-time plot of  $\eta$  at midgap shows the complicated wobbles



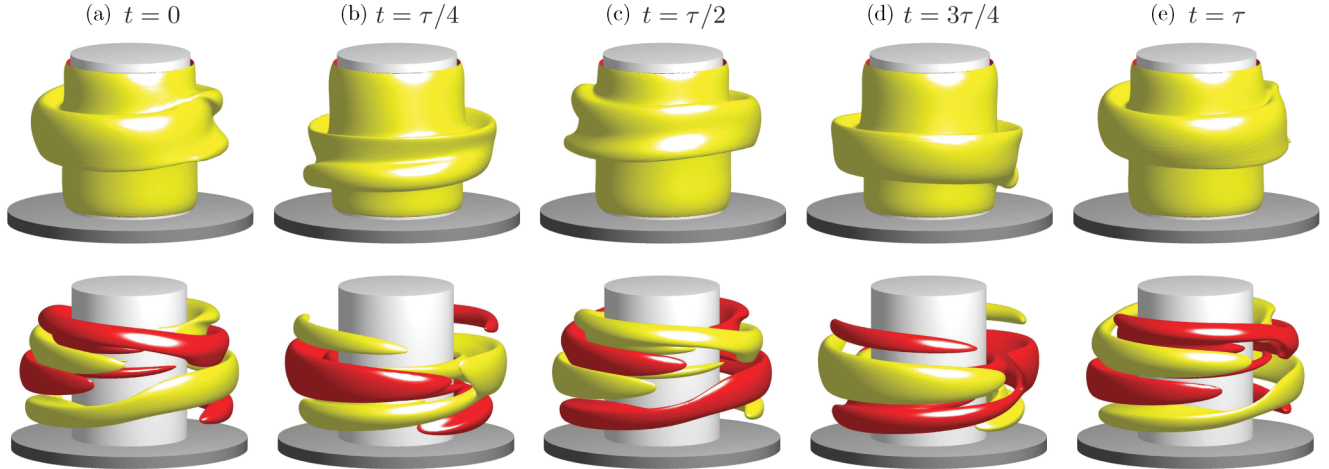


FIG. 29. (Color online) Isosurfaces of  $rv$  of the full solution (top row,  $rv = 300$ ) and of the  $m = 1$  contribution (bottom row,  $rv = \pm 30$ ) at five different times  $t$  as indicated over a time period  $\tau = 0.188$  for  $T_2^a$  at  $Re_i = 410$ .

in the interior (see Fig. 30 for  $q_2^a$  at  $Re_i = 410$  and Fig. 21 for  $q_3$  at  $Re_i = 400$ ).

## VII. DISCUSSION AND CONCLUSION

The numerical simulations of the small-aspect-ratio wide-gap counterrotating Taylor-Couette system have revealed a sequence of symmetry-breaking Hopf bifurcations as the inner cylinder rotation is increased. The dynamics are dominated by the centrifugal instability of the angular momentum distribution in the inner cylinder boundary layer. This holds even for the first instability, which is usually considered to be shear driven in classical treatments of the counterrotating system with large (or infinite) aspect ratio. The small aspect

ratio and the corresponding end wall effect change the classical scenario: For slow inner cylinder rotations, a reflection symmetric jet of angular momentum emerges from the inner cylinder boundary layer at midplane. The flow is steady, axisymmetric, and reflection symmetric about the midplane. This basic state undergoes an axisymmetric Hopf bifurcation to a periodic state  $l$  in which additional small jets erupt from the inner cylinder boundary layer and the primary jet no longer emerges from the midplane but oscillates about it, resulting in a flow that is half-period-flip symmetric. For higher inner cylinder rotations,  $l$  becomes unstable, spawning a two-frequency state  $q_2^s$ . One of the frequencies  $\omega$  corresponds to the frequency of the underlying  $l$  from which it bifurcated and the new frequency corresponds to a mean precession of the  $m = 1$  component and is seen as a wobble of the jets. The 2-torus  $T_2^s$  on which the flows  $q_2^s$  reside retains all the spatial symmetries of the system, but the mean precession destroys the half-period-flip invariance of  $q_2^s$ . However,  $q_2^s$  remains invariant to a spatial-temporal symmetry whose action consists of that of the half-period-flip symmetry composed with an additional rotation about the axis by a small drift angle. Faster inner cylinder rotations increase the amplitudes of the wobbles and another Hopf bifurcation introduces a third incommensurate frequency and flows on a 3-torus  $T_3^s$ . The 3-torus is destroyed with increasing inner cylinder rotation as the third frequency vanishes at a SNIC bifurcation where the reflection symmetry is broken. Following this, quasiperiodic solutions evolve on one or other symmetrically related 2-tori  $T_2^a$  and  $T_2^{a*} = K_z T_2^a$ .

In unraveling this sequence of symmetry-breaking bifurcations and characterizing the solutions and the spaces in which they exist, we have had to make use of a combination of tools: first, an accurate Navier-Stokes solver, but then having the solutions they needed to be characterized in order to relate them to the corresponding equivariant normal form theory. In problems with symmetries and in particular spatiotemporal symmetries, we have found it necessary to utilize both local and global measures of the flow state. Our study shows that the characteristics of the flow at different locations are very different: the flow appears almost axisymmetric at the inner cylinder

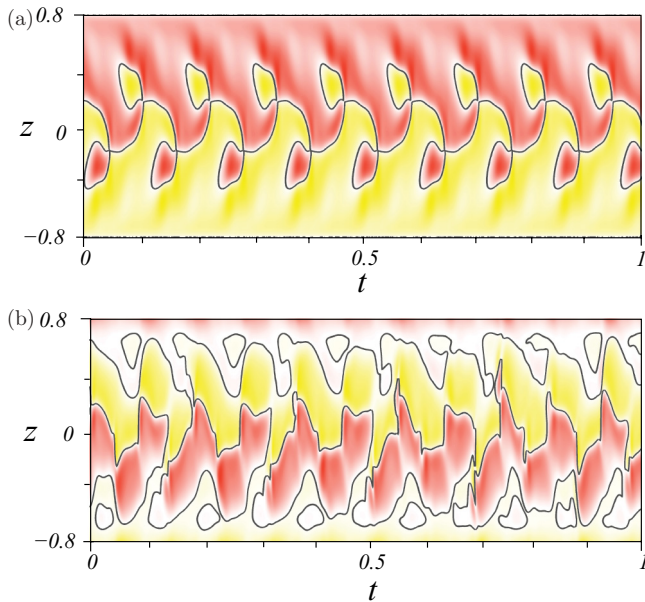


FIG. 30. (Color online) Space-time plot of  $\eta$  for  $q_2^a$  at midgap over one diffusion time at  $Re_i = 410$ . Red (dark gray) and yellow (light gray) correspond to positive and negative values, with (a)  $\eta \in [-1720, 1720]$  and (b)  $\eta \in [-950, 950]$ .

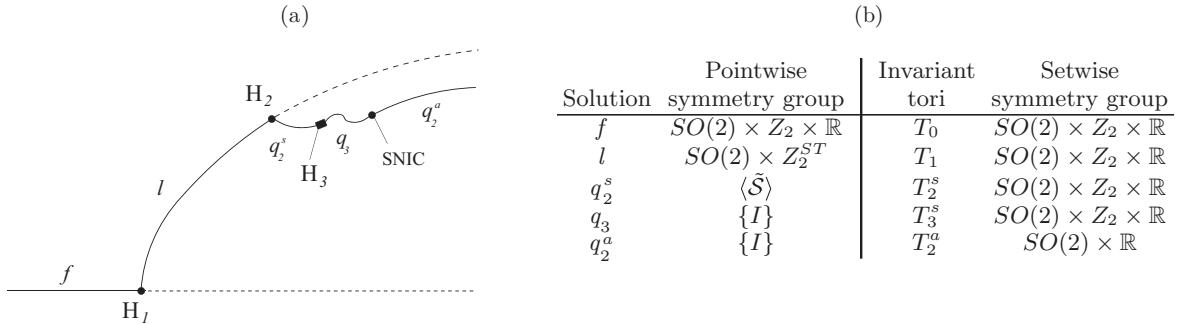


FIG. 31. (a) Schematic bifurcation diagram, using  $Re_i$  as the bifurcation parameter. Here  $H_1$  is a Hopf bifurcation of the basic state  $f$  spawning the limit cycle  $l$ . At the Hopf bifurcation  $H_2$ , a quasiperiodic symmetric state  $q_2^s$  emerges out of the limit cycle  $l$  and subsequently undergoes another Hopf bifurcation  $H_3$  spawning a quasiperiodic  $q_3$ . In  $q_3$ , a SNIC bifurcation takes place, leading to asymmetric solutions  $q_2^a$  and  $q_2^{a*}$ . Stable (unstable) solution branches are shown as solid (dashed) curves. (b) Pointwise and setwise symmetry groups of the stable solutions found and the corresponding invariant tori where they exist. The components  $\mathbb{R}$ ,  $Z_2^{ST}$ , and  $\langle \tilde{\mathcal{S}} \rangle$  are generated by symmetries involving time; the other components consist of purely spatial symmetries.

and the succession of bifurcations do not modify it. However, at the cylinder midgap all the bifurcations and symmetry breakings are clearly identified, as we have seen from the time series at both locations (Figs. 8, 18, 21, and 30). Something similar happens when looking at local and global measurements, such as time series at a given point (a local measure) and the kinetic energy of the Fourier modes (global measures), which reflect different flow properties. The fast Fourier transform of the modal energies and of the time series we have analyzed display different properties of the flow. Both kinds of measurements (different physical locations, local or global) are important and complementary, and focusing on just one of them can be misleading. Therefore, experiments and numerical simulations of complicated flows must be carefully conducted, examining all of these characteristics and then rationalizing the results in terms of equivariant normal form theory.

A schematic of the bifurcation sequences discussed above, with increasing  $Re_i$ , is shown in Fig. 31(a). Figure 31(b) lists the pointwise symmetry groups of all the solutions obtained and also the setwise symmetry groups of the associated invariant tori where these solutions exist. The pointwise symmetry groups of the solutions are reduced at each bifurcation as some of the symmetries are broken until finally  $q_3$  and  $q_2^a$  do not have any remaining symmetry. Their symmetry group is  $\{I\}$  consisting of a single element, the identity transformation. The associated invariant tori, however, retain all the symmetries of the governing equations, i.e., they are invariant as a set when the symmetries are applied, except for  $T_2^a$ , which loses the reflection symmetry  $K_z$ . The invariant tori  $T_n$ , where  $n$  is the dimension of the torus, contain a continuous family of different solutions, except for the lower-dimensional ones, which contain a single solution:  $T_0 = f$  and  $T_1 = l$ . The symmetry breaking at each bifurcation is summarized as follows. At  $H_1$  the base state  $f$ , which is invariant under the full symmetry group of the problem,  $SO(2) \times Z_2 \times \mathbb{R}$ , loses stability and a limit cycle  $l$  is spawned, breaking the  $K_z$  symmetry and the time invariance  $\phi_t$  of the steady state  $f$ . The limit cycle, however, is invariant to a combination of the two broken symmetries, consisting of  $K_z$  composed with a half-period time translation. This half-period-flip symmetry

$\mathcal{S}$  and the rotational symmetries  $R_\alpha$  are then broken in the Hopf bifurcation of maps  $H_2$  and only their combination  $\tilde{\mathcal{S}}$ , a new spatiotemporal symmetry of the bifurcated quasiperiodic solution  $q_2^s$ , remains. Then all pointwise symmetries are broken in a secondary Hopf bifurcation of maps  $H_3$ , spawning a three-frequency quasiperiodic solution  $q_3$ . Considered as sets, all the invariant tori created at the three successive Hopf bifurcations preserve the full symmetry group of the problem  $SO(2) \times Z_2 \times \mathbb{R}$ . Finally, in the SNIC bifurcation, the setwise reflection symmetry  $K_z$  is broken. The  $K_z$ -symmetric  $T_3$  is destroyed and two different two-tori  $T_2^a$  and  $T_2^{a*}$  result. These are symmetrically related:  $K_z T_2^a = T_2^{a*}$ .

Symmetry-breaking SNIC bifurcations in small-aspect-ratio Taylor-Couette flows between a symmetric 2-torus (modulated rotating waves) and a symmetrically related 1-tori (rotating waves) have been observed experimentally and numerically [50–52]. An analogous  $Z_2$  symmetry-breaking SNIC bifurcation has also been found in rotating convection [53], again with the SNIC bifurcation taking place on a symmetric 2-torus and the saddles and nodes involved being conjugate pairs of 1-tori (rotating wave states). In another very-small-aspect-ratio Taylor-Couette flow with only the inner cylinder rotating, a similar SNIC bifurcation was found numerically to occur on a 3-torus with the saddle nodes being  $Z_2$ -conjugate 2-tori (modulated rotating waves) [46] and there is experimental evidence that is suggestive of the existence of the 3-torus involved [8,9].

Similar bifurcations not of the solutions, but of some invariant sets such as low-dimensional tori or strange attractors have been reported in other problems and in particular in chaotic or even turbulent flows. These bifurcations can be symmetry breaking or symmetry restoring and may play an important role in the transition to turbulence and in the characterization of the different turbulent states [54–56]. It has also been suggested that reversals of the geomagnetic poles may be explained in terms of symmetry-breaking SNIC bifurcations in a turbulent setting [57–59].

Taylor-Couette flow at small aspect ratios has shown itself to be a good paradigm for studying symmetry-breaking bifurcations and for the study of not only the solutions but also more

complex low-dimensional objects: invariant tori and attractors. These studies can improve our understanding of the transition to turbulence and it is worthwhile continuing the study of geometrically simple and well-posed canonical systems such as Taylor-Couette flow at small aspect ratio in this regard.

## ACKNOWLEDGMENTS

This work was funded by the Korea Science and Engineering Foundation World Class University Grant No. R32-2009-000-20021-0 and the Spanish government Grant No. FIS2009-08821.

- 
- [1] G. I. Taylor, *Philos. Trans. R. Soc. London Ser. A* **223**, 289 (1923).
- [2] P. Chossat and G. Iooss, *The Couette-Taylor Problem* (Springer, Berlin, 1994).
- [3] T. B. Benjamin, *Proc. R. Soc. London Ser. A* **359**, 1 (1978).
- [4] T. B. Benjamin, *Proc. R. Soc. London Ser. A* **359**, 27 (1978).
- [5] K. A. Cliffe, J. J. Kobine, and T. Mullin, *Proc. R. Soc. London Ser. A* **439**, 341 (1992).
- [6] T. B. Benjamin and T. Mullin, *Proc. R. Soc. London Ser. A* **377**, 221 (1981).
- [7] M. Lücke, M. Mihelcic, K. Wingerath, and G. Pfister, *J. Fluid Mech.* **140**, 343 (1984).
- [8] G. Pfister, H. Schmidt, K. A. Cliffe, and T. Mullin, *J. Fluid Mech.* **191**, 1 (1988).
- [9] G. Pfister, A. Schulz, and B. Lensch, *Eur. J. Mech. B* **10**(2), 247 (1991).
- [10] G. Pfister, T. Buzug, and N. Enge, *Physica D* **58**, 441 (1992).
- [11] F. Marques and J. M. Lopez, *J. Fluid Mech.* **561**, 255 (2006).
- [12] K. A. Cliffe, *J. Fluid Mech.* **135**, 219 (1983).
- [13] A. Schulz, G. Pfister, and S. J. Tavener, *Phys. Fluids* **15**, 417 (2003).
- [14] R. J. Donnelly and D. Fultz, *Proc. R. Soc. London Ser. A* **258**, 101 (1960).
- [15] C. D. Andereck, S. S. Liu, and H. L. Swinney, *J. Fluid Mech.* **164**, 155 (1986).
- [16] M. Golubitsky and I. Stewart, *SIAM J. Math. Anal.* **17**, 249 (1986).
- [17] D. Coles, *J. Fluid Mech.* **21**, 385 (1965).
- [18] A. Prigent, G. Gregoire, H. Chate, O. Douchot, and W. van Saarloos, *Phys. Rev. Lett.* **89**, 014501 (2002).
- [19] J. Antonijoin, F. Marques, and J. Sanchez, *Phys. Fluids* **10**, 829 (1998).
- [20] A. Goharzadeh and I. Mutabazi, *Eur. Phys. J. B* **19**, 157 (2001).
- [21] S. Dong, *J. Fluid Mech.* **615**, 371 (2008).
- [22] S. Dong, *Phys. Rev. E* **80**, 067301 (2009).
- [23] A. Meseguer, F. Mellibovsky, M. Avila, and F. Marques, *Phys. Rev. E* **79**, 036309 (2009).
- [24] A. Meseguer, F. Mellibovsky, M. Avila, and F. Marques, *Phys. Rev. E* **80**, 046315 (2009).
- [25] R. van Hout and J. Katz, *Phys. Fluids* **23**, 105102 (2011).
- [26] S. Hughes and A. Randriamampianina, *Int. J. Numer. Methods Fluids* **28**, 501 (1998).
- [27] I. Mercader, O. Batiste, and A. Alonso, *Comput. Fluids* **39**, 215 (2010).
- [28] J. M. Lopez and J. Shen, *J. Comput. Phys.* **139**, 308 (1998).
- [29] M. Avila, M. Grimes, J. M. Lopez, and F. Marques, *Phys. Fluids* **20**, 104104 (2008).
- [30] M. Avila, *Phys. Rev. Lett.* **108**, 124501 (2012).
- [31] T. Mullin and C. Blohm, *Phys. Fluids* **13**, 136 (2001).
- [32] J. M. Lopez, F. Marques, and J. Shen, *J. Fluid Mech.* **51**, 327 (2004).
- [33] J. M. Lopez, *Phys. Fluids* **7**, 2700 (1995).
- [34] A. Hirsa, J. M. Lopez, and S. Kim, *Exp. Fluids* **29**, 309 (2000).
- [35] See Supplemental Material at <http://link.aps.org/supplemental/10.1103/PhysRevE.86.046316> for movies showing (a) contours of  $rv$  at  $Re_i = 300$  in T1\_Rei300.avi (corresponding to Fig. 3), (b) contours of  $rv$  at  $Re_i = 320$  in T1\_Rei320.avi (corresponding to Fig. 7), (c) isosurfaces of  $rv$  at  $Re_i = 365$  for the full solution in T2s\_Rei365.avi and the  $m = 1$  contribution in T2s\_Rei365\_m1.avi (corresponding to Fig. 12), (d) the same as the  $m = 1$  movie in (c) but strobed, (e) contours of the  $m = 1$  contribution to  $rv$  for  $Re_i = 365$  in T2s\_Rei365\_z-cut.avi, and (f) isosurfaces of  $rv$  at  $Re_i = 400$  for the full solution in T3\_Rei400.avi and the  $m = 1$  contribution in T3\_Rei400\_m1.avi (corresponding to Fig. 20).
- [36] F. Marques, J. M. Lopez, and H. M. Blackburn, *Physica D* **189**, 247 (2004).
- [37] Y. A. Kuznetsov, *Elements of Applied Bifurcation Theory*, 3rd ed. (Springer, New York, 2004).
- [38] S. Strogatz, *Nonlinear Dynamics and Chaos* (Addison-Wesley, Reading, MA, 1994).
- [39] M. Field and M. Golubitsky, *Notices of the AMS* **42**(2), 240 (1995).
- [40] M. Golubitsky and I. Stewart, *The Symmetry Perspective: From Equilibrium to Chaos in Phase Space and Physical Space* (Birkhäuser, Basel, 2002).
- [41] J. D. Crawford and E. Knobloch, *Annu. Rev. Fluid Mech.* **23**, 341 (1991).
- [42] J. M. Lopez and F. Marques, *Phys. Rev. Lett.* **85**, 972 (2000).
- [43] F. Marques, J. M. Lopez, and J. Shen, *Physica D* **156**, 81 (2001).
- [44] F. Marques, J. M. Lopez, and V. Iranzo, *Phys. Fluids* **14**, L33 (2002).
- [45] M. Avila, F. Marques, J. M. Lopez, and A. Meseguer, *J. Fluid Mech.* **590**, 471 (2007).
- [46] J. M. Lopez and F. Marques, *Phys. Rev. E* **68**, 036302 (2003).
- [47] J. M. Lopez, *J. Fluid Mech.* **553**, 323 (2006).
- [48] J. M. Lopez and F. Marques, *J. Fluid Mech.* **628**, 269 (2009).
- [49] C. Grebogi, E. Ott, and J. A. Yorke, *Phys. Rev. Lett.* **51**, 339 (1983).
- [50] J. Abshagen, J. M. Lopez, F. Marques, and G. Pfister, *Phys. Rev. Lett.* **94**, 074501 (2005).
- [51] J. Abshagen, J. M. Lopez, F. Marques, and G. Pfister, *J. Fluid Mech.* **540**, 269 (2005).
- [52] J. Abshagen, J. M. Lopez, F. Marques, and G. Pfister, *J. Fluid Mech.* **613**, 357 (2008).
- [53] A. Rubio, J. M. Lopez, and F. Marques, *J. Fluid Mech.* **608**, 357 (2008).
- [54] L. Bordja, L. S. Tuckerman, L. M. Witkowski, M. C. Navarro, D. Barkley, and R. Bessaih, *Phys. Rev. E* **81**, 036322 (2010).

- [55] N. Mujica and D. P. Lathrop, [Physica A \*\*356\*\*, 162 \(2005\)](#).
- [56] N. Mujica and D. P. Lathrop, [J. Fluid Mech. \*\*551\*\*, 49 \(2006\)](#).
- [57] M. Berhanu, R. Monchaux, S. Fauve, N. Mordant, F. Pétrélis, A. Chiffaudel, F. Daviaud, B. Dubrulle, L. Marié, F. Ravelet, M. Bourgoin, P. Odier, J.-P. Pinton, and R. Volk, [Europhys. Lett. \*\*77\*\*, 59001 \(2007\)](#).
- [58] F. Ravelet, R. Monchaux, S. Aumaître, A. Chiffaudel, F. Daviaud, B. Dubrulle, M. Bourgoin, P. Odier, N. Plihon, J.-P. Pinton, R. Volk, S. Fauve, N. Mordant, and F. Pétrélis, [Phys. Rev. Lett. \*\*101\*\*, 074502 \(2008\)](#).
- [59] F. Pétrélis, S. Fauve, E. Dormy, and J.-P. Valet, [Phys. Rev. Lett. \*\*102\*\*, 144503 \(2009\)](#).